IVYSPRING INTERNATIONAL PUBLISHER

Theranostics

2027; 17(2): 818-844. doi: 10.7150/thno.141156

Research Paper

Bioinspired ultrasound-responsive piezoelectric topological patches with controlled magnesium release and immunomodulation for bone defect repair

Zhengwei Liu[1,2], Hui Zhang[3], Yu Wang[3,4]✉, Yuanjin Zhao[3]✉, Yongxiang Wang[1,2]✉

1. Department of Orthopedics, Northern Jiangsu People's Hospital, 225001, Yangzhou, China.
2. Department of Orthopedics, Northern Jiangsu People's Hospital, Clinical Teaching Hospital of Medical School, Nanjing University, 225001, Yangzhou, China.
3. Department of Rheumatology and Immunology, Nanjing Drum Tower Hospital, School of Biological Science and Medical Engineering, Southeast University, 210096, Nanjing, China.
4. Zhejiang Key Laboratory of Soft Matter Biomedical Materials, Wenzhou Institute, University of Chinese Academy of Sciences, Wenzhou, Zhejiang, 325000, China.

✉ Corresponding authors: Email: yuwang@wiucas.ac.cn (Y. Wang); yjzhao@seu.edu.cn (Y.J. Zhao); wangyongxiang@nju.edu.cn (Y.X. Wang).

© 2027 The Author(s). This is an open access article distributed under the Creative Commons Attribution 4.0 International Licence, subject to the Publisher's Terms of Use at https://ivyspring.com/terms.

Received: 2026.07.19; Accepted: 2026.10.20; Published: 2027.01.01

Abstract

Rationale: Bone defect repair demands spatiotemporal coordination of bioactive cues, yet current patches lack precise control and mechanistic insight. We developed a bio-inspired ultrasound (US)-responsive piezoelectric topological patch integrating controllable magnesium ion (Mg^{2+}) release and immunomodulation.

Methods: β-PVDF-Mg patches with micro-nano topography were fabricated and characterized for piezoelectricity and Mg^{2+} release kinetics. Osteogenesis, angiogenesis, macrophage polarization, and cranial bone defect repair in rats were assessed, with transcriptomic analysis.

Results: The patch exhibited US-triggered piezoelectric output and US-triggered and externally controlled Mg^{2+} release (from 28.1% to 93.6% with US). It directed cell alignment, enhanced osteogenic differentiation, promoted angiogenesis, reduced reactive oxygen species (ROS), and drove M2 macrophage polarization (arginase-1 (Arg-1) ↑ and nitric oxide synthase (iNOS) ↓). *In vivo*, it significantly improved bone regeneration (bone mineral density (BMD), bone volume/tissue volume (BV/TV) and collagen) and M2 polarization. Transcriptomic and phosphorylation analyses identified PI3K-AKT and MAPK-ERK signaling as candidate regulatory pathways, and pharmacological inhibition of either pathway attenuated the β-PVDF-Mg+US-induced reparative macrophage phenotype and reduced the pro-osteogenic activity of macrophage-conditioned medium.

Conclusions: The multimodal patch provides a US-responsive platform that integrates piezoelectric stimulation, Mg^{2+} release, and topographical guidance to promote a regenerative osteoimmune microenvironment, with PI3K-AKT and MAPK-ERK signaling functionally contributing to macrophage regulation and downstream osteogenic paracrine effects.

Keywords: US; piezoelectric effect; topological structure; immunomodulation; bone repair

Introduction

Effective regeneration of substantial bone defects requires tightly coordinated inflammatory resolution, vascular ingrowth, osteogenic differentiation, and matrix mineralization [1, 2]. Among the biochemical regulators involved in these processes, magnesium ion (Mg^{2+}) can influence both osteogenic cells and the local immune microenvironment [3-5]. However, its biological efficacy is strongly dependent on local concentration and exposure duration, making uncontrolled release undesirable [6-9]. Most Mg-containing biomaterials rely on degradation- or diffusion-driven ion liberation and therefore provide limited external control over release kinetics. A material system capable of coupling remotely regulated Mg^{2+} delivery with regenerative physical cues may therefore offer greater temporal control over the bone-healing microenvironment [10-13].

Herein, we present a novel bio-inspired ultrasound (US)-responsive piezoelectric topological patch with controllable Mg^{2+} release and

immunomodulation for bone defect repair, as schemed in **Figure 1**. Recent piezoelectric biomaterials have demonstrated that mechanical or externally applied stimuli can be converted into localized electrical cues to promote bone regeneration [14-16]. More recently, piezoelectricity has also been combined with bioactive ion delivery. However, we chose Poly(vinylidene fluoride) (PVDF) over degradable poly(L-lactic acid) (PLLA) and poly(3-hydroxybutyrate-co-3-hydroxyvalerate) (PHBV) because its non-degradability ensures stable β-phase piezoelectric output for sustained US-triggered Mg^{2+} release, preserves surface topography for contact guidance, and avoids acidic degradation byproducts that cause inflammation and hinder Mg^{2+} mineralization. Thus, PVDF is a stable actuator, and its permanence is essential for our long-term strategy. The present study aimed to establish a US-responsive interface integrating piezoelectric electrical stimulation, enhanced Mg^{2+} release, and surface topographical guidance to cooperatively regulate cell fate.

In this paper, we constructed a type of piezoelectric topological patches with desired properties, including US-triggered and externally adjustable Mg^{2+} delivery, conductivity, immunomodulatory capacity to improve defected bone repair. To mimic the oriented arrangement of collagen fibers that guide cell growth and differentiation, α-phase PVDF patches with defined patterning structures were prepared through an imprinting technique while Mg^{2+} was encapsulated to form α-PVDF-Mg composites. Subsequent thermal annealing followed by immediate ice-water quenching, together with $MgCl_2 \cdot 6H_2O$-assisted crystallization and electrical poling, promoted the formation and stabilization of an electroactive β-phase-rich PVDF structure [17], yielding β-PVDF-Mg patches with significantly enhanced piezoelectric response, which provides the foundation for on-demand electrical stimulation of US-triggered piezoelectric responses. Notably, β-PVDF-Mg patches enabled US-triggered piezoelectric output and externally adjustable Mg^{2+} release. In combination with the surface topography, these effects promoted osteogenic differentiation and angiogenesis through immunomodulation. It is the precise integration of all these elements into a single, stable platform that constitutes our core advance. The β-PVDF-Mg patch with US stimulation effectively accelerated the bone repair through immunomodulation *in vivo*, and ribonucleic acid (RNA) transcriptome sequencing reveals osteogenesis-related immunomodulatory mechanisms. These findings indicate that the US-responsive piezoelectric topological patches with controllable Mg^{2+} release and immunomodulation hold great promise for applications in bone defect repair. As summarized in **Table S2**, the key distinction of our design is not merely integrating multiple functional components, but functionally coupling topographical guidance, piezoelectric electrical stimulation, and US-triggered and externally adjustable Mg^{2+} release into a unified spatiotemporally coordinated therapeutic system.

Materials and Methods

Materials

PVDF (Mw ≈ 350,000, CAS: P1492342, aladdin); dimethylformamide (DMF, analytical grade) (≥ 99.5%, CAS: 68-12-2, aladdin); magnesium chloride hexahydrate ($MgCl_2 \cdot 6H_2O$, ≥ 99%, CAS: 7791-18-6, aladdin); mouse embryo osteoblast precursor cells (MC3T3-E1); minimum essential medium α (α-MEM medium) (BioReagent, CAS: M1370044, aladdin); dulbecco's modified eagle medium (DMEM) cell culture medium (BioReagent, CAS: D1372055, aladdin); cell live dead stain kit (CAS: C2015S, Beyotime); senescence β-Galactosidase (CAS: C0602, Beyotime); masson's trichrome stain kit (CAS: G1346, Solarbio); superoxide dismutase 1 (SOD1) staining kit (CAS: K107203P, Solarbio); anuokang biotech (Nanjing, China) provided the male sprague-dawley (SD) rats.

Preparation of β-PVDF-Mg patches

PVDF homopolymer powder (8 g) was dissolved in DMF (40 mL) under continuous stirring for 12 h to obtain a homogeneous 20% (w/v) PVDF solution. $MgCl_2 \cdot 6H_2O$ was then added to the PVDF/DMF solution and stirred to prepare a transparent and homogeneous PVDF-Mg precursor solution. The solution was cast onto glass substrates bearing the linear topographical pattern and dried at 70 ℃ for 1 h. The as-prepared PVDF-Mg films were carefully peeled from the substrates and annealed at 140 ℃ for 24 h, and immediately quenched in ice water to promote crystalline reorganization and retention of the electroactive phase. The films were subsequently electrically poled under the specified polarization conditions to further align the polar dipoles. The resulting electroactive films were referred to as β-PVDF-Mg patches. Their crystalline structures were subsequently characterized by X-ray diffractometer (XRD) meter (Bruker D8 Advanced) and Fourier-transform infrared spectroscopy (FTIR).

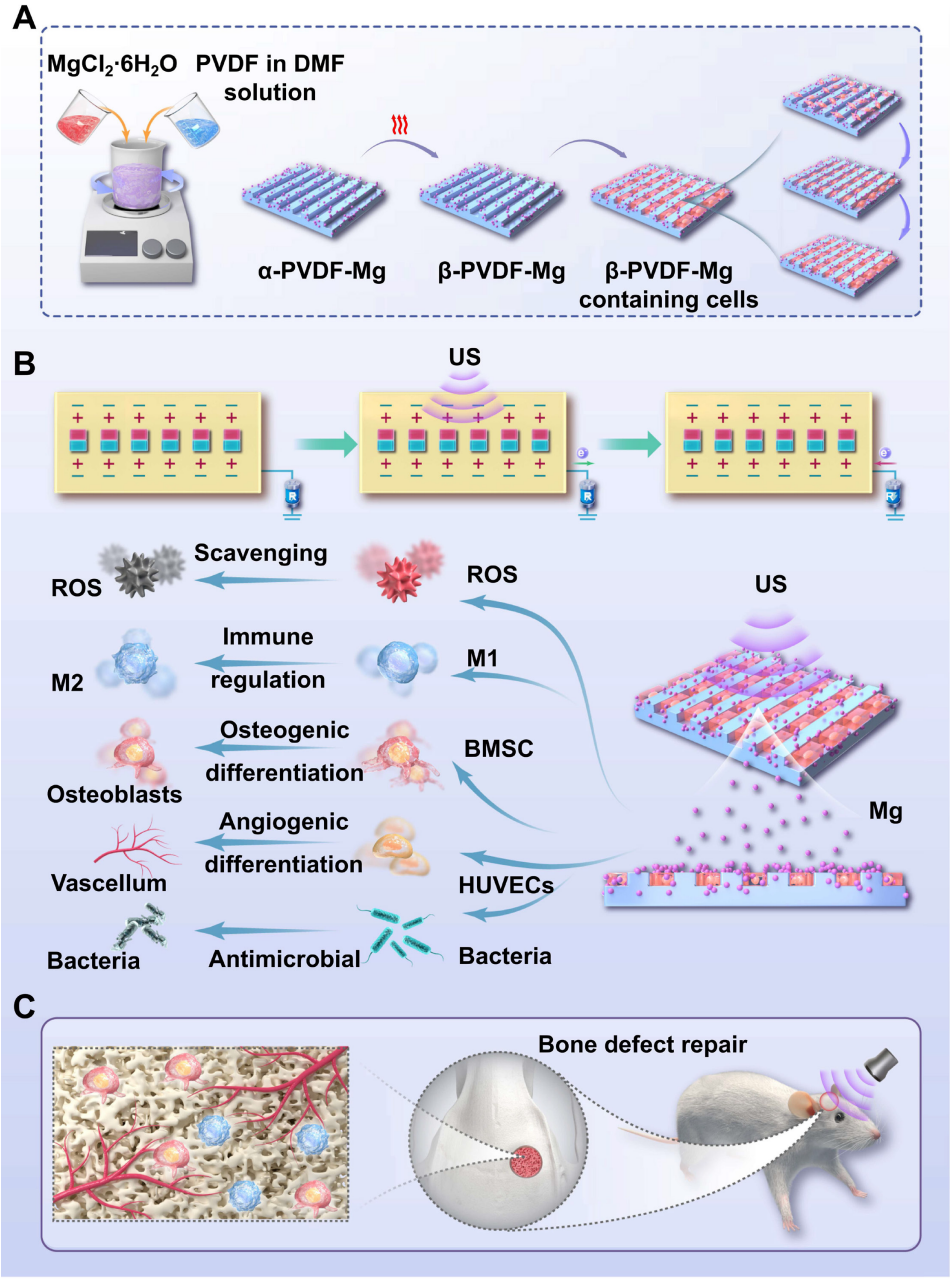


Figure 1. Schematic illustration of β-PVDF-Mg patches for bone defect repair. (A) Preparation procedure of the β-PVDF-Mg patches. **(B, C)** Mechanism of responsive β-PVDF-Mg patches integrating US stimulation on bone defects.

Structural and property characterization of β-PVDF-Mg patches

For 3D reconstruction and thickness measurement, β-PVDF-Mg patches were immersed in rhodamine solution for 24 h to enhance confocal contrast. This staining is non-specific: the fluorescence arises from electrostatic adsorption of cationic rhodamine B onto the negatively charged PVDF surface (due to its fluorinated backbone), rather than from selective labelling of any component. Surface morphology of the β-PVDF-Mg patches was characterized using scanning electron microscopy (SEM) (Zeiss, Merlin). An XRD meter was used to measure the crystal structures in patches, and the XRD patterns of β-PVDF can be indexed. Furthermore, the ferroelectric polarization versus electric field curves of β-PVDF-Mg patches were characterized by a ferroelectric tester (radiant multiferroic): the d_{33} values of the β-PVDF-Mg patches (the piezoelectric coefficient d_{33} of β-PVDF and β-PVDF-Mg patches was measured using a piezoelectric coefficient tester under identical conditions. The samples were cut into 10 × 10 mm pieces with a thickness of approximately 35 μm. During measurement, the samples were sandwiched between Au electrodes, and an oscillating mechanical

force of 0.25 N was applied with 110 Hz frequency. The d_{33} values were calculated from the generated charge response under a poling voltage of 1500 V at room temperature) and polarization-electric (P-E) hysteresis loops of the β-PVDF-Mg patches (the electric field was swept over approximately - 60 to + 60 kV/cm at room temperature) were measured by a commercial d_{33} meter (ZJ-4AN) and ferroelectric analyzer (FE-3000), separately. The US-responsive piezoelectric output was recorded using an oscilloscope and US exciters. To evaluate the effect of plasma-assisted surface hydrophilization, β-PVDF and β-PVDF-Mg patches were treated using a CPC-E plasma system with oxygen as the working gas. The oxygen flow rate was maintained at 200 mL/min, the plasma power was set to 60 W, and the treatment duration was 3 min. The water contact angles (WCA) of untreated and plasma-treated patches were subsequently measured using a WCA analyzer (VCA OPTIMA, AST). The stress-strain curves of different thicknesses of β-PVDF-Mg patches were recorded by a tensile instrument (MTS Standard 43) (compression rate: 5 mm/min) and repeated 3 times. For Mg^{2+} release characterization, 5-mm-diameter β-PVDF-Mg patches containing 0.05 mmol elemental Mg per patch (approximately 1.215 mg Mg per patch, corresponding to 6.19 mg/cm²) were used, consistent with the formulation employed in the cellular and *in vivo* experiments. Individual patches were immersed in 5 mL double distilled H_2O (ddH_2O) and subjected to the indicated US stimulation regimen. Aliquots were collected and appropriately diluted before inductively coupled plasma-mass spectrometry (ICP-MS) (Agilent 7700X) analysis. Cumulative Mg^{2+} release was calculated after correction for the Mg^{2+} removed during sequential sampling.

Cell proliferation and apoptosis detection

MC3T3-E1 grew in the α-MEM (HyClone). Cells were inoculated with different patches (Control, Control+US, β-PVDF, β-PVDF+US, β-PVDF-Mg, β-PVDF-Mg+US). Here, the Control group refers to β-PVDF patches without micro-nano linear topology, while the Control+US group refers to β-PVDF patches without micro-nano linear topology under US stimulation. This was the case in all subsequent experimental groups. Cellular proliferation was quantified using the cell counting kit-8 (CCK-8) assay (Beyotime, C0038). Similarly, after the cells have been treated for three days, MC3T3-E1 apoptosis was detected using flow cytometry (FACSCanto, BD, USA).

Cell morphology assay

MC3T3-E1 were seeded onto different kinds of patches for 7 days. After 7 days of culture, cells were stained to show their morphology. Briefly, after fixation in 4% PFA and blocking with 1% bovine serum albumin (BSA) (2 h), cells were stained with phalloidin (30 min, 25 ℃) and DAPI (5 min) sequentially. Cell orientation was then detected using a fluorescence microscope (Leica, M205 FA) and quantified using ImageJ.

Osteogenic induction and detection

Osteogenic differentiation of MC3T3-E1 was evaluated using complementary phenotypic and molecular assays. Alkaline phosphatase (ALP) activity was assessed after 14 days of culture, and extracellular matrix mineralization was examined by alizarin red s (ARS) staining on day 21. Expression of osteocalcin (OCN), osteopontin (OPN) and collagen type I (Col-I) was evaluated by immunofluorescence (IF), with nuclei counterstained using DAPI. In parallel, RNA was isolated for reverse transcription-qPCR (RT-qPCR) analysis of osteogenesis-related genes, with glyceraldehyde-3-phosphate dehydrogenase (*GAPDH*) used for normalization (with primers detailed in Supplemental **Table S1**). Imaging data were acquired under identical conditions and quantified using ImageJ.

Assay of MC3T3-E1 migration

The β-PVDF patches and β-PVDF-Mg patches were placed on the bottom and MC3T3-E1 was cultured on the top of the polycarbonate membrane using transwell. MC3T3-E1 was cultured at 37 °C, during which the patches were stimulated with US. Migrating cells stained with crystal violet were captured, and analyzed with ImageJ.

SA-β-Gal staining of MC3T3-E1 after different treatments

2% paraformaldehyde (PFA) fixed MC3T3-E1 for 5 min. Following phosphate buffered saline (PBS) rinses, SA-β-Gal staining proceeded at 37 ℃ (16 h). Washed samples underwent light microscopy imaging, with senescent cells quantified.

Human umbilical vein endothelial cells (HUVECs) migration assay

A previously described scratch assay [18] was used to evaluate HUVECs migration. After cell attachment, the corresponding US stimulation was applied according to the experimental grouping. Cell migration was subsequently evaluated to explore the combined effects of the surface topography, piezoelectric stimulation, and Mg^{2+} release. The images of each group of HUVECs were captured by fluorescence microscopy and analyzed with ImageJ.

Tube formation assay

To assess angiogenesis of HUVECs with β-PVDF-Mg patches in a co-culture system, tube formation assays were performed. HUVECs were seeded onto the matrigel-coated wells to initiate capillary-like tube formation. And the patches were carefully positioned over the HUVECs layer cultured on the matrigel surface. The corresponding US stimulation was subsequently applied, and tube formation was evaluated after incubation.

In vitro antioxidant activity of β-PVDF-Mg patches

The function of the β-PVDF-Mg patches to clear reactive oxygen species (ROS) was assessed in RAW264.7. H_2O_2 (200 μM) was then added to each group for 48 h. 2′, 7′-dichlorodihydrofluorescein diacetate (DCFH-DA) was dipped in fresh medium, and the pictures were captured in 24-well plates using fluorescence microscope after 20 min.

RAW264.7 cell morphology assay

After fixation (4% PFA, 15 min) and PBS wash, cell permeabilization (5 min) and blocking (5% BSA, 30 min) were performed. F-actin and nuclear staining followed published methods.

IF staining of RAW264.7

RAW264.7 cells were cultured with different treatments (Control, Control+US, β-PVDF, β-PVDF+US, β-PVDF-Mg and β-PVDF-Mg+US). The staining protocol is described as follows: 1. primary antibodies (1:100), (4 ℃ overnight); 2. secondary antibodies [FITC-conjugated, Alexa Fluor® 594-conjugated] (60 min); 3. nuclear staining: DAPI (5 min).

Flow cytometric analysis of macrophage phenotype

RAW264.7 macrophages were cultured under the indicated treatment conditions (Control, Control+US, β-PVDF, β-PVDF+US, β-PVDF-Mg, and β-PVDF-Mg+US). After collection, cells were immunostained for CD86 and CD206. FlowJo v10.8.1 was used to calculate the percentages of CD86 and CD206 macrophages. Three independent experiments were conducted.

Antimicrobial performance testing

The β-PVDF-Mg was examined against *S. aureus* and *E. coli*. Each bacterial suspension (10 μL, 1×10^8 CFU/mL) was introduced into wells containing the indicated samples. US was applied for 5 min to the designated groups. Following treatment, bacteria were recovered in 1 mL PBS, and 20 μL aliquots were plated for viable-colony determination after 18 h at 37 °C. Five independent replicates were analyzed, and morphological alterations of the bacteria were examined by SEM.

Animal model establishment

Under aseptic conditions, a 4-mm bone defect was created in the right parietal bone using a circular hollow drill, and completely covered with a 5-mm sterilized circular patch (ethics approval numbers: 2024AE02018). Penicillin was administered intramuscularly for 3 postoperative days. Rats received different intervention (Control, Control+US, β-PVDF, β-PVDF+US, β-PVDF-Mg and β-PVDF-Mg+US). For groups receiving US, US was delivered transcutaneously using sterile coupling gel with the transducer centered over the defect. Animals were sacrificed at 8 weeks. Calvarial specimens were harvested for micro-CT and histological analyses: IF and immunohistochemistry (IHC). For histological evaluation, sections were obtained using consistent anatomical orientation across all specimens. Histological staining were quantitatively analyzed within the entire original 4 mm defect region using identical regions of interest (ROI).

To determine the residual Mg content after long-term implantation, β-PVDF-Mg patches retrieved after 8 weeks were carefully collected and processed for quantitative Mg analysis. Unimplanted β-PVDF-Mg patches from the same batch were used to determine the initial Mg content. After nitrolytic cleavage, ICP-MS is used to detect Mg content. Residual Mg content was expressed as the amount of Mg remaining in each retrieved patch relative to that in the corresponding unimplanted patch.

Transcriptome sequencing and analysis

RAW264.7 cells were cultured with different treatment (48 h), with the latter receiving a 20-min US exposure once per day. Cells were lysed with trizol for latter RNA sequencing.

Phosphorylation-specific enzyme-linked immunosorbent assay (ELISA)

RAW264.7 cells were lysed after specified treatment and the levels of phosphorylated AKT (p-AKT), p-AKT/AKT, phosphorylated ERK (p-ERK), and p-ERK/ERK were quantified using phosphorylation-specific ELISA kits. Activation of the PI3K-AKT and MAPK-ERK pathways was evaluated using the p-AKT/AKT and p-ERK/ERK ratios.

Pathway inhibition and IF analysis

To assess the functional involvement of PI3K-AKT and MAPK-ERK signaling in β-PVDF-Mg+US-

induced macrophage regulation, PI3K inhibitor (LY294002, 10 μM) or the MEK1/2 inhibitor (U0126, 10 μM) inhibited RAW264.7 cells before corresponding treatment. Then, cells were assigned to the Control, β-PVDF-Mg+US, β-PVDF-Mg+US+LY294002, and β-PVDF-Mg+US+U0126 groups. IF staining was then performed for p-AKT, p-ERK1/2, arginase-1 (Arg-1) and nitric oxide synthase (iNOS), with DAPI nuclear counterstaining. ImageJ was used to quantify fluorescence intensity from images collected under consistent acquisition parameters.

Macrophage-conditioned medium-mediated osteogenic assay

To evaluate whether PI3K-AKT- and MAPK-ERK-dependent macrophage responses contributed to downstream osteogenesis, conditioned media were collected from RAW264.7 cells in the Control, β-PVDF-Mg+US, β-PVDF-Mg+US+LY294002, and β-PVDF-Mg+US+U0126 groups. After centrifugation (1000 rpm, 5 min), the conditioned media were used to culture MC3T3-E1 for 7 days. Recombinant runt-related transcription factor 2 (RUNX2) and OPN expression served as osteogenic readouts and was examined by IF. Fluorescence signals were measured with ImageJ using images collected under standardized acquisition parameters.

Experimental group definitions

Control group: smooth β-PVDF patches without micro-nano linear topography or Mg incorporation and received no US stimulation; Control+US group: smooth β-PVDF patches but received US stimulation; β-PVDF group: β-PVDF patches with micro-nano linear topography but without Mg incorporation or US stimulation; β-PVDF+US group: β-PVDF patches with micro-nano linear topography and US stimulation. β-PVDF-Mg group: β-PVDF patches containing both micro-nano linear topography and Mg incorporation without US stimulation; β-PVDF-Mg+US group: β-PVDF patches containing both micro-nano linear topography and Mg incorporation with US stimulation (**Table S6**).

US stimulation protocol

Low-intensity pulsed ultrasound (LIPUS) stimulation was delivered using a transducer with a center frequency of 1.5 MHz. The US intensity was set at 30 mW/cm² (the corresponding US output power is 0.6 W) (**Table S7**), with a frequency of 1.0 kHz and a duty cycle of 20% [19-21]. Unless otherwise specified, all biological assays were completed within 20 min per session, administered once daily. (The selected frequency, intensity, duty cycle, and daily treatment duration are comparable to commonly used noninvasive LIPUS regimens for bone-healing applications [22].)

For *in vitro* experiments, the transducer was positioned directly beneath the center of the corresponding culture well with the acoustic axis aligned with the center of the corresponding well, and the transducer-to-sample distance was maintained at 3 mm, and US coupling gel was used to provide reproducible acoustic coupling between the transducer and the culture plate. The culture medium volume was maintained at 2 mL per well to provide a constant acoustic propagation path during all experiments. Because reflections from the liquid–air interface and culture-plate boundaries can generate standing-wave patterns in multi-well systems, medium depth, transducer–sample spacing, transducer orientation, sample position and acoustic path length were kept identical for all experimental groups. Peripheral wells were not used for quantitative experiments, and samples were positioned in central wells to minimize exposure to the peripheral portion of the transducer beam and reduce potential transducer edge effects. Acoustic attenuation through the culture-plate bottom, coupling layer, and culture medium was not assumed to be negligible. Therefore, the reported intensity represents the nominal output condition of the US system rather than an independently mapped intracavity pressure field within each well. All experimental comparisons were consequently performed using an identical plate type, coupling configuration, transducer–sample distance, medium volume, and transducer alignment to minimize variability in the effective acoustic exposure and US–piezoelectric coupling efficiency. To evaluate potential thermal effects, the temperature of the sample environment was monitored during the 20-min LIPUS treatment under the same acoustic parameters used for the biological experiments. Corresponding sham-treated samples without US exposure served as thermal controls.

Use of artificial intelligence tools

ChatGPT (OpenAI) was used as an auxiliary language-editing tool during manuscript revision, primarily for grammatical correction, improvement of sentence structure, and refinement of wording in the manuscript and responses to reviewers. The tool was not used for experimental design, primary data acquisition, generation of experimental results, or independent scientific interpretation.

Statistical analysis

Mean values with standard deviations are reported for quantitative measurements. Statistical processing was completed in Origin 2024, with the

Shapiro–Wilk test applied to assess distributional normality and Levene's test used to determine whether variances were comparable across groups. For datasets meeting the required parametric assumptions, group comparisons were carried out by one-way ANOVA with subsequent Tukey testing. Statistical significance was accepted at $p < 0.05$. Unless otherwise stated, cell experiments included no fewer than three independent biological replicates, and four animals were assigned to each experimental group. Technical measurements obtained within the same biological replicate were averaged before statistical testing. For the *in vivo* experiment, four animals were included in each of the six treatment groups. A post hoc sensitivity analysis for a one-way ANOVA (six groups, total n = 24, α = 0.05) indicated that this design provided 80% power to detect an overall effect size of approximately Cohen's f = 0.85. Therefore, the study was primarily powered to detect large between-group effects. Given the limited sample size, the study was not specifically powered for all intermediate pairwise comparisons, and non-significant pairwise results were therefore interpreted cautiously and not considered evidence of equivalence.

Results and Discussion

The β-PVDF-Mg patches demonstrate US-responsive piezoelectric effect

The confocal reconstruction revealed the thickness of β-PVDF-Mg patches, which suggested that we prepared piezoelectric topological β-PVDF-Mg patches via imprinting technology, with tunable thickness control (**Figure S1A and Figure 2A**). The SEM result demonstrated a highly integrated micro-nano linear topology pattern on the patch surface (**Figure 2B**), with a groove width of 350 ± 62 nm, a ridge width of 400 ± 87 nm, and a groove depth of 306 ± 59 nm (**Table S3**). These dimensions fall within the range previously reported to promote osteogenesis via contact guidance (e.g., 200-400 nm ridge/groove patterns). The energy dispersive spectroscopy (EDS) mapping indicated successful incorporation of Mg^{2+} (**Figure S1B**). XRD analysis examined the crystal conformation of β-PVDF-Mg. Distinct α and β phases were observed in the α-PVDF, β-PVDF and β-PVDF-Mg patches respectively, with the highest diffraction peak occurring at $2\theta \approx 20.6^{o}$ on the crystal planes of the β ferroelectric phase (**Figure 2D**). XRD quantitative analysis (**Table S4**) confirmed the formation of an electroactive β-phase-rich PVDF structure after thermal annealing, rapid quenching, and subsequent poling. The β-PVDF and β-PVDF-Mg samples exhibited a dominant diffraction peak at approximately $2\theta = 20.6^{o}$, corresponding predominantly to the overlapping (110)/(200) reflections of β-PVDF. Incorporation of $MgCl_2 \cdot 6H_2O$ resulted in a slight shift of the β-phase peak from 20.56^{o} to 20.60^{o} and a decrease in FWHM from 0.997^{o} to 0.969^{o}, suggesting modest changes in crystalline ordering. As previous reports, hydrated $MgCl_2$ can act as a nucleating species and influence the formation of polar crystalline phases in PVDF [23]. Because the β-phase enrichment was modest, we do not attribute the electroactive structure to $MgCl_2$ incorporation alone; rather, it likely reflects the combined effects of salt-assisted nucleation, thermal treatment, rapid quenching, and electrical poling [24]. FTIR further supported the presence of the electroactive β-phase. The characteristic absorption band near 1275 cm^{-1}, together with the strong electroactive-phase-associated band near ~840 cm^{-1}, was observed in β-PVDF and β-PVDF-Mg, whereas characteristic α-phase bands near 763, 795, and 976 cm^{-1} were diminished (**Figure 2E**). The phase assignment was therefore based on the combined XRD and FTIR results rather than on any single vibrational band [23, 25]. The FTIR spectra of β-PVDF-Mg and pristine β-PVDF were nearly identical, showing no significant shifts in the characteristic absorption peaks or the appearance of new peaks that would indicate chemical bonding or changes in the polymer's chemical structure. This strongly suggested that Mg^{2+} is physically incorporated within the PVDF matrix rather than covalently bonded to the polymer backbone, serving as bioactive ion reservoirs for US-regulated release.

Significantly, the resulting β-PVDF-Mg patch exhibited an excellent US-triggered piezoelectric effect, where US stimulation induced charge separation between internal/external surfaces and accelerated interfacial charge release, thereby generating electrical signals (**Figure 2C**). The d_{33} of α-PVDF, β-PVDF and β-PVDF-Mg were 1.2, 14 and 19 pC/N, respectively, based on triplicate measurements from ten sample points (**Figure 2F**). The β-PVDF-Mg patch exhibited a closed polarization-electric field hysteresis loop over an electric-field range of approximately - 60 to + 60 kV/cm (**Figure 2G**). The presence of finite remanent polarization and coercive-field crossings supports field-induced polarization switching of the electroactive PVDF matrix. A moderate asymmetry was observed between the positive and negative branches, which may be related to electrode-polymer interfacial effects and asymmetric charge accumulation or injection within the ferroelectric fluoropolymer system [26, 27]. The leakage current profile showed an initial capacitive charging spike upon field application, followed by a rapid decay to stable leakage level, reflecting good

insulation performance (**Figure S1D**). The low leakage current is in accordance with the insulating nature of the PVDF matrix and may reflect suppressed charge transport associated with space-charge redistribution, electrode injection and field-dependent conduction processes in ferroelectric polymers [28-30]. Overall, the β-PVDF-Mg sample demonstrated a typical ferroelectric hysteresis loop with low leakage current, highlighting its potential for piezoelectric device applications. Furthermore, we detected by an electronic oscilloscope that the output voltages on both sides were close to 0 without US stimulation, but increased with US intensity while maintaining temporal synchronization with stimulation periods (**Figure 2H**). Such charge releasing and output voltage of the β-PVDF-Mg patches will provide the basis for non-invasive and localized electrical stimulation of adherent cells, thereby affecting cellular behaviors. To investigate the degradability of the β-PVDF-Mg patch, the degradation test *in vivo* was conducted through implanting it in animals for 8 weeks. As shown in the **Figure S2A**, SEM results indicated that the micro-nano linear topological structure on the patch surface remained clearly visible. Compared to before implantation, the mass of the β-PVDF-Mg patch did not undergo significant change (**Figure S2B**). These indicated that the β-PVDF-Mg patch was not prone to degradation and exhibited excellent structural stability. Meanwhile, the d_{33} constant and US response performance of β-PVDF-Mg patches implanted in animals for 8 weeks were evaluated. In contrast to the β-PVDF-Mg patch before implantation, the d_{33} of the β-PVDF-Mg patches showed a slight decrease and remained at 16 pC/N (**Figure S2C**), and the slight reduction in d_{33} may be caused by the changes in the local composite microenvironment following gradual Mg^{2+} release, while the dominant β-phase PVDF crystalline structure remained preserved. And the β-PVDF-Mg patch's output voltage gradually increased with rising US intensity (**Figure S2D**). The results indicated that the β-PVDF-Mg patch maintained superior piezoelectric properties and US response performance, even after long-term implantation in the body. The preserved piezoelectric performance is primarily attributed to the stable β-phase crystalline structure and non-degradability of PVDF, which remained intact after implantation. Importantly, maintaining stable piezoelectric output throughout the healing process enables sustained US-triggered electrical stimulation together with controllable Mg^{2+} release, thereby continuously supporting macrophage polarization, osteogenesis, angiogenesis, and subsequent bone remodeling during long-term bone regeneration. Finally, this non-biodegradable characteristic allows the β-PVDF-Mg patch to maintain favorable biocompatibility within the investigated period *in vivo*.

Although the β-PVDF-Mg patch maintained structural integrity and piezoelectric functionality during the 8-week implantation period, this endpoint represents only an early-to-intermediate stage of bone healing in the rat cranial defect model and is insufficient to establish long-term biocompatibility of permanently retained PVDF. Because PVDF is non-resorbable, prolonged cranial retention may potentially result in delayed fibrous encapsulation, chronic foreign-body reactions, or persistent low-grade inflammation that may not become apparent within the present observation window. Therefore, extended implantation studies with detailed local histological assessment will be indispensable to evaluate whether permanent retention is clinically acceptable. If long-term retention proves undesirable, secondary surgical retrieval or the use of removable implant architectures may be required. Alternatively, future generations of the platform could employ biodegradable piezoelectric polymers such as PLLA or PHBV, which may provide electromechanical stimulation during the regenerative phase while reducing the long-term burden associated with a permanently retained synthetic polymer [31-35].

We examined the performance of β-PVDF-Mg patches by tensile tester. As shown in **Figure S1A**, **E**, the maximum axial tensile force of the β-PVDF-Mg patches gradually increased as their thickness increases. When the thickness of the β-PVDF-Mg patch was 35 μm, its maximum axial tensile force reached 11 N, which fully satisfies the mechanical support for large cranial bone defect repair [36, 37]. Moreover, hydrophilic biomaterial surfaces have been reported to attenuate pro-inflammatory macrophage responses and promote a pro-healing osteoimmune microenvironment [38, 39]. As shown in **Figure S1C**, **F**, the WCA value of the β-PVDF-Mg patch (72.55°) was smaller than that of the β-PVDF patch (90.37°), attributable to the addition of Mg^{2+}. Oxygen plasma treatment further enhanced surface wettability, reducing the WCA of β-PVDF-Mg from 72.55° to 19.43°, which may be beneficial for subsequent cell-material interactions. To evaluate the release behavior of Mg^{2+} from β-PVDF-Mg under US triggering, we examined the cumulative release of Mg^{2+} using ICP-MS. To characterize Mg^{2+} release under biologically relevant loading conditions, release experiments were performed using the same high-loading β-PVDF-Mg formulation for studies (*in vitro* and *in vivo*) (1.215 mg elemental Mg per 5-mm patch; 6.19 mg/cm²). As observed in **Figure 2I,** the cumulative release of Mg^{2+} increased with repeated US irradiation cycles, reaching 93.6% (absolute cumulative amount of Mg^{2+}:

1.137 mg), while the cumulative release amount of Mg^{2+} from β-PVDF-Mg was only around 28.1% (absolute cumulative amount of Mg^{2+}: 0.342 mg) without US irradiation. So Mg^{2+} from β-PVDF-Mg could be controlled by US as an external regulatory cue rather than merely an auxiliary stimulus. **Figure S2E** revealed a clear correlation between the Mg^{2+} release kinetics and US intensities that the cumulative release of Mg^{2+} increased progressively with increasing US intensity over an identical stimulation period. To establish the relevance between therapeutic LIPUS condition and piezoelectric regulation of Mg^{2+} release, we further correlated US intensity with the voltage generated by the β-PVDF-Mg patch. At the biological LIPUS intensity of 30 mW/cm², the patch generated an output voltage of approximately 160 mV (**Figure S2D, F**). This voltage therefore represents the biologically relevant piezoelectric output generated during the treatments. Consistent with this observation, voltage-dependent release experiments demonstrated enhanced Mg^{2+} release at comparable piezoelectric potentials (160 mV) (**Figure S2G**), supporting the hypothesis that the piezoelectric potential generated during LIPUS stimulation contributes to regulation of Mg^{2+} release [40]. A detailed comparison of the two datasets revealed an important nuance that the total cumulative Mg^{2+} release in **Figure S2E** (direct US stimulation) was consistently slightly higher than that in **Figure S2G** (equivalent voltage stimulation alone) across all intensity/voltage pairs. Rather than serving solely as an electrical stimulation platform, the piezoelectric β-PVDF-Mg patch also functions as an active regulator of Mg^{2+} release: US-induced piezoelectric polarization dynamically modulates Mg^{2+} release kinetics, thereby coupling electrical and biochemical cues within a single therapeutic platform. Recent advances in externally regulated biomaterials have demonstrated increasing levels of therapeutic programmability. For example, Yin et al. developed a near-infrared regulated multi-mode periosteum scaffold capable of sequentially coordinating antibacterial, immunomodulatory, and regenerative functions through different irradiation strategies [41]. In comparison, the present β-PVDF-Mg platform employs a single US stimulus to activate coupled electromechanical and ionic responses. Rather than independently switching multiple therapeutic modules, our system provides an externally triggered and adjustable regenerative cue by synchronizing piezoelectric stimulation with Mg^{2+} release.

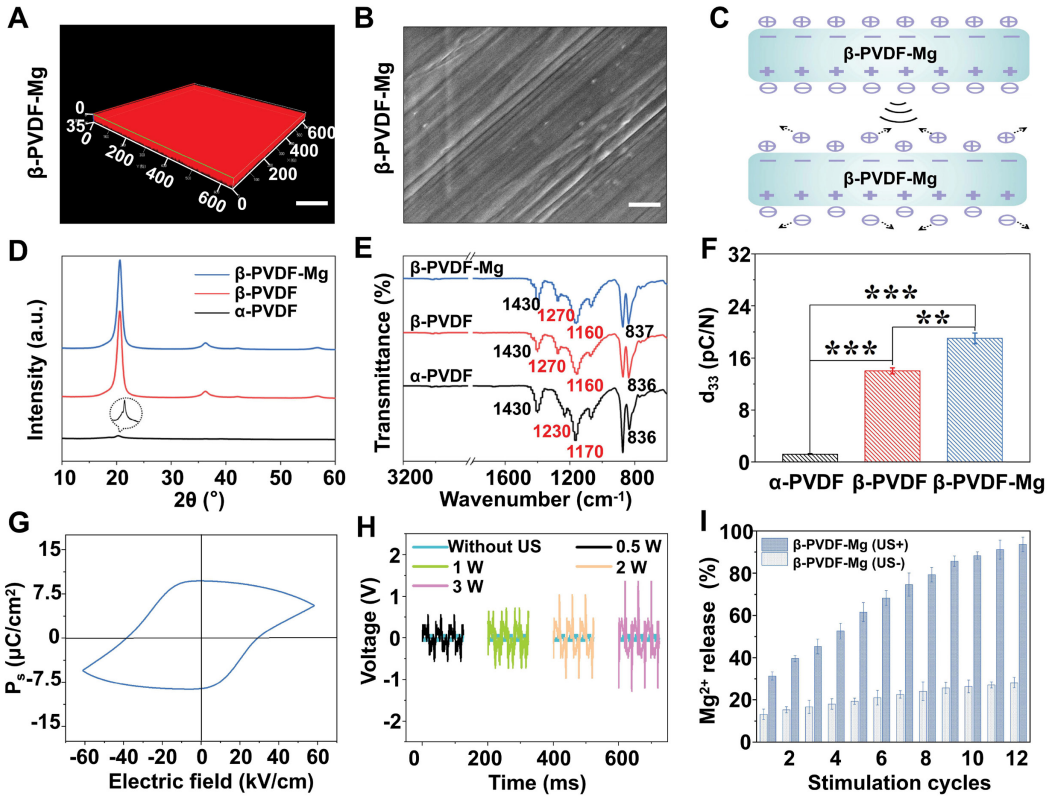


Figure 2. Characterization of the β-PVDF-Mg patches. (A) 3D LSCM reconstruction of the rhodamine-stained β-PVDF-Mg patch used for thickness measurement; scale bar: 100 μm. **(B)** SEM picture of β-PVDF-Mg; scale bar: 2 μm. **(C)** Illustration of the US-triggered piezoelectric effect of β-PVDF-Mg patches. **(D)** XRD patterns of α-PVDF, β-PVDF and β-PVDF-Mg patches. **(E)** FTIR spectra of α-PVDF, β-PVDF and β-PVDF-Mg patches. **(F)** The d_{33} constant of α-PVDF, β-PVDF and β-PVDF-Mg (n = 3 for each group). **(G)** P-E hysteresis loops for β-PVDF-Mg patch. **(H)** Piezoelectric output voltage of β-PVDF-Mg patches under different acoustic output powers of the US transducer (0.5-3 W). The effective radiating area of the transducer was approximately 20 cm², corresponding to nominal area-averaged acoustic intensities of approximately 25-150 mW/cm². **(I)** US-responsive Mg^{2+} release under repeated stimulation cycles (n = 3 for each group). The power of US was 30 mW/cm². Data are reported as mean ± SD from three biologically independent experiments. Group differences were analyzed by one-way ANOVA with Tukey's post hoc test; $^{**}p < 0.01$ and $^{***}p < 0.001$.

Therefore, the current platform represents a simplified US-responsive strategy that enables dynamic modulation of the local osteoimmune microenvironment, while further development toward stage-specific or independently programmable therapeutic regulation remains an important future direction.

The β-PVDF-Mg patches demonstrate biocompatibility and induce directed cell growth

We co-cultured MC3T3-E1 with β-PVDF-Mg patches to evaluate the cytocompatibility of the various patches. The result indicated low cytotoxicity of β-PVDF substrate, US stimulation, piezoelectric microcurrents and Mg^{2+} (**Figure S3A-C**). Interestingly, the biocompatibility was more positive in the β-PVDF+US and β-PVDF-Mg+US groups that received US stimulation, compared to the β-PVDF and β-PVDF-Mg groups without US stimulation. Of note, the β-PVDF-Mg+US group exhibited the most pronounced increase in proliferation rate, suggesting a synergistic effect of US stimulation, piezoelectric effect and Mg^{2+}. In addition, the apoptosis rate in β-PVDF-Mg+US was 1.99% (**Figure S4A-H**). The results suggest that US-stimulated β-PVDF-Mg conferred enhanced cell viability to MC3T3-E1, facilitating subsequent tissue regeneration.

Periosteum covering bones comprises an outer fibrous layer where collagen fibers exhibit directional alignment, most pronounced in the diaphysis [42-44]. Previous studies have confirmed that natural periosteum of the backbone exhibits longitudinal fiber orientation. Likewise, lamellar bone harbors osteoblast networks characterized by strong directional alignment and intricate connectivity [45]. Therefore, the highly integrated micro-nano linear topology pattern on the surface of β-PVDF-Mg patches theoretically is capable of replicating the directional alignment of collagen fibers characteristic of native periosteum [46, 47]. To investigate such topological influence on cellular behavior, we cultured MC3T3-E1 for 5 days on both micro-nano linear patterned and non-patterned β-PVDF surfaces, analyzing cell orientation, aspect ratio, and elongation (**Figure 3A**). SEM and phalloidin/DAPI staining revealed distinct morphological differences between different groups. On non-patterned β-PVDF patch surface, MC3T3-E1 displayed random orientation. In contrast, cells grown on topological surfaces across all experimental groups (β-PVDF, β-PVDF+US, β-PVDF-Mg, β-PVDF-Mg+US) exhibited excellent directional alignment along the linear topological pattern (**Figure 3B, C**). Quantitative orientation analysis demonstrated that cells on the patterned surfaces exhibited a pronounced orientation peak at approximately 90^o in our image-based angular coordinate system, whereas cells on the non-patterned control surfaces showed a broadly distributed orientation over 0^o–180^o. In this coordinate system, 0^o was the horizontal image axis, while the long axis of the micro-nano grooves was oriented at approximately 90^o. Therefore, the orientation peak near 90^o represents preferential cell alignment parallel to the groove axis (**Figure 3D-H**). This directional preference was further confirmed by $\sin\alpha^o$ measurements of actin alignment orientation (**Figure 3I**). In addition, compared to the irregularly growing MC3T3-E1, oriented aligned MC3T3-E1 had increased aspect ratios and cellular elongation, as well as improved cell areas (**Figure 3J-L**). These findings provide clear evidence that MC3T3-E1 are mechanosensitive to linear topological patterns, preferentially aligning along the engineered micro-nano grooves in a manner that mimics their natural orientation in periosteal tissue [48-50].

The β-PVDF-Mg patches demonstrate pro-osteogenic effects *in vitro*

The osteogenic process involves two critical phases: osteoblast differentiation coupled with bone matrix mineralization typically assessed through ALP activity assays and quantification of bone mineralization nodules (BMNs) [51-53]. As exhibited in **Figure 4A, B**, ALP and BMN (ARS staining) expression across these groups, indicated that we successfully induced MC3T3-E1 into osteoblasts with osteogenic differentiation ability, as well as that the β-PVDF patch itself did not inhibit the osteogenic behavior *in vitro*. Quantitative analysis revealed the β-PVDF-Mg+US group exhibited highest ALP and BMN expression (**Figure 4G, H**), implying that β-PVDF-Mg patch with US stimulation could effectively promote osteogenesis. Notably, US-treated groups (β-PVDF+US and β-PVDF-Mg+US groups) showed significantly enhanced ALP and BMN staining compared to non-US-treated groups (β-PVDF and β-PVDF-Mg groups), which could be attributed to piezoelectric effect promoting cellular differentiation. In addition, the β-PVDF patch with linear topological pattern exhibited a higher level of ALP/BMN expression versus blank controls, confirming the pro-osteogenic effect of guided cellular alignment.

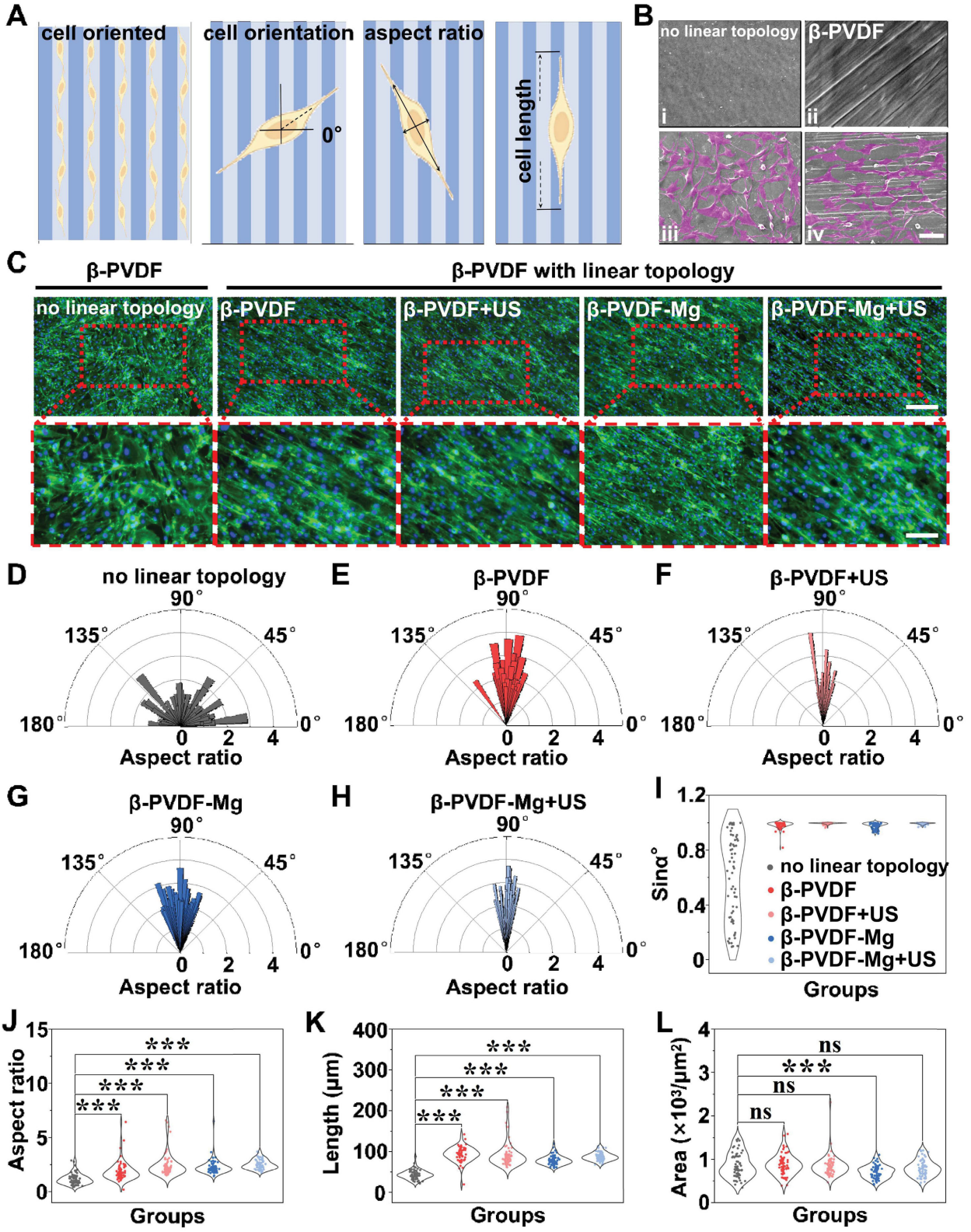


Figure 3. Directed Growth of MC3T3-E1 on β-PVDF-Mg patches. (A) Illustration of MC3T3-E1 directional growing on β-PVDF-Mg patch with micro-nano linear topology, along with parameter measurement methods. **(B)** SEM images of β-PVDF-Mg patch without **(i)** and with **(ii)** micro-nano linear topologies, as well as SEM images of MC3T3-E1 grown on β-PVDF-Mg patch without **(iii)** and with **(iv)** micro-nano linear topologies; scale bar: 50 μm. **(C)** Fluorescent images of MC3T3-E1 growing on β-PVDF (topological β-PVDF) and β-PVDF-Mg patches with and without micro-nano linear topologies (n = 3). The scale bars represent 100 μm (top) and 50 μm (bottom). Green: phalloidin; Blue: DAPI. For the polar plots in (**D–H**), the orientation angle was defined relative to the horizontal image axis (0°). The long axis of the micro-nano grooves was positioned at approximately 90°; therefore, an orientation peak around 90° indicates alignment parallel to the groove direction. **(I)** Quantification of MC3T3-E1 orientation using sinα, where α is the cell orientation angle relative to the horizontal image axis and the principal groove axis is defined as 90°. Values approaching 1 indicate alignment parallel to the grooves, whereas values approaching 0 indicate greater deviation toward a perpendicular orientation (n = 3, 3 analyzed areas per n). **(J-L)** Statistical analysis of aspect ratio **(J)**, cell length **(K)** and cell area **(L)** of MC3T3-E1 grown on different substrates. Data are mean ± SD from three biologically independent replicates; one-way ANOVA: ns, not significant; ***$p < 0.001$.

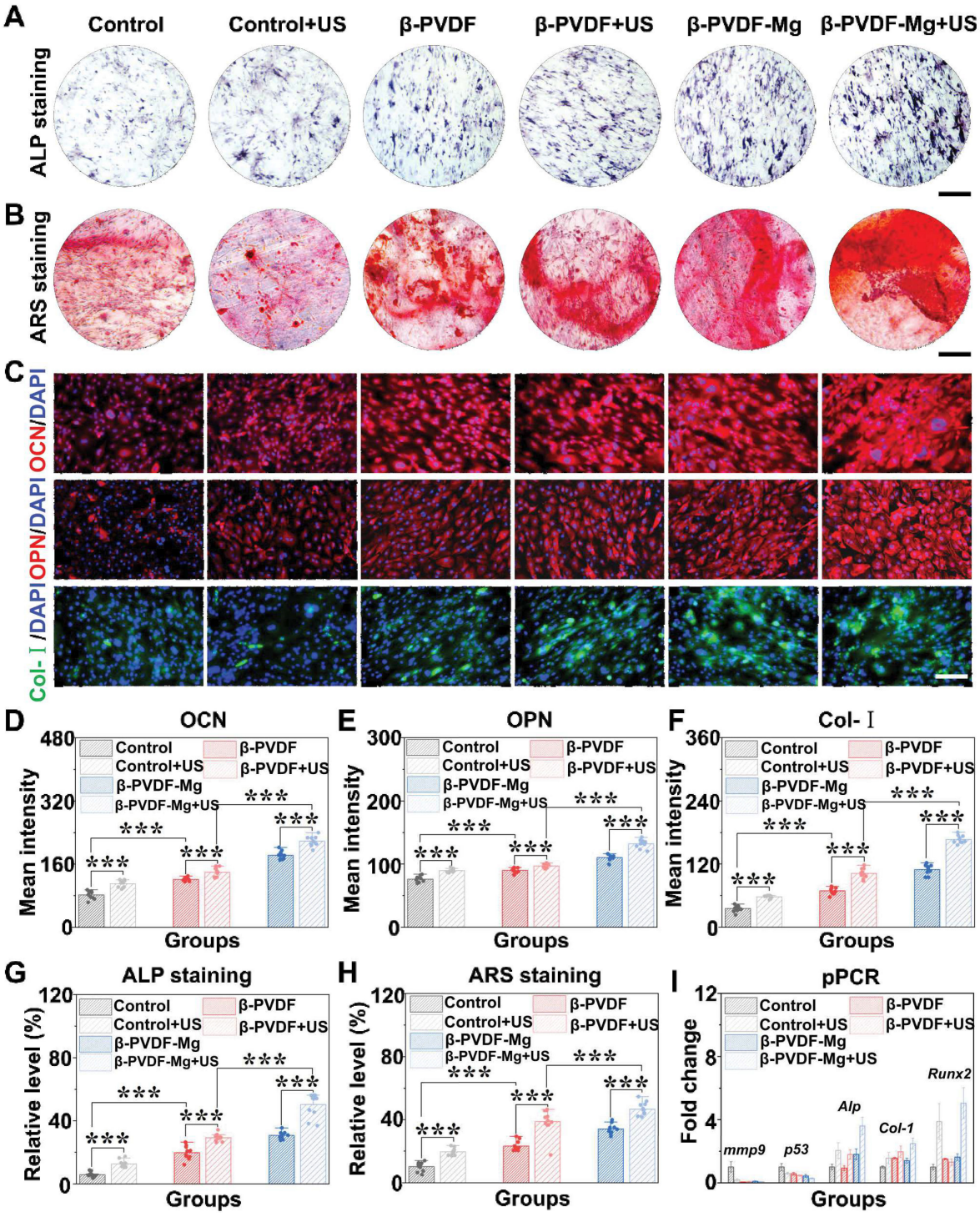


Figure 4. Pro-osteogenesis effect of β-PVDF-Mg patches. (A, B) ALP and ARS staining performed after osteogenic induction, showing early osteogenic activity and matrix mineralization, respectively. Images were obtained from 24-well plates (n = 3); scale bar: 4 mm. **(C)** IF detection of OCN, OPN, and Col-I in MC3T3-E1 on day 7 (n = 3); scale bar: 80 μm. **(D-F)** Quantitative analysis for OCN, OPN, and Col-I, respectively (n = 3). **(G, H)** Densitometric quantification of ALP and ARS staining, respectively (n = 3). **(I)** RT-qPCR assessment of osteogenesis-related gene expression (n = 3). The Control group consisted of smooth β-PVDF patches lacking micro-nano linear topography. Data are mean ± SD from three biologically independent replicates; one-way ANOVA: ***$p < 0.001$.

OCN and OPN are major non-collagenous bone matrix proteins associated with osteoblast maturation and mineralization, whereas Col- I constitutes the principal organic framework of bone matrix [54-56]. **Figure 4C** showed that IF staining revealed markedly enhanced expression of OCN, OPN and Col-I in the β-PVDF-Mg+US group. Under identical control conditions, the US-stimulated β-PVDF-Mg group (i.e., β-PVDF-Mg+US group) exhibited significantly higher expression levels of OCN, OPN and Col-I, compared

to the β-PVDF-Mg group without US stimulation (i.e., β-PVDF-Mg group), which may be ascribed to the piezoelectric effect stimulating osteoblast differentiation (**Figure 4D-F**). Similarly, under the presence of US stimulation, the β-PVDF-Mg containing Mg^{2+} group (i.e., β-PVDF-Mg+US group) exhibited higher expression of OCN, OPN and Col-I compared to the Mg^{2+}-free β-PVDF group (i.e., β-PVDF+US group), which was related to the Mg^{2+}. Therefore, we concluded that the most pronounced osteogenic activity observed in all experimental groups was due to the synergistic biological effects of piezoelectric effect and Mg^{2+} release. Moreover, the β-PVDF group with linear topological pattern also exhibited a higher expression level of osteogenesis-related proteins, which was consistent with the ALP and ARS staining results described above. All these results may be attributed to the topological pattern, piezoelectric effect and Mg^{2+} release [57-63]. At the level of gene transcription, the genes (*Alp*, *Runx2* and *Col-I*) expression were highest in the β-PVDF-Mg+US group, demonstrating the beneficial impact of β-PVDF-Mg with US stimulation on promoting bone formation (**Figure 4I**). Because Mg^{2+} released from β-PVDF-Mg by piezoelectric effect could promote MC3T3-E1 differentiation. In addition, the β-PVDF-Mg+US treatment also resulted in lower expression of the tumor suppressor gene *p53* and the matrix-remodeling gene *mmp9* (**Figure 4I**), indicating treatment-associated changes in stress-response and matrix-remodeling gene expression. These results revealed that β-PVDF-Mg with US stimulation had great potential in accelerating osteogenic process.

Biological effects related to bone regeneration of the β-PVDF-Mg patches

To explore the homing on MC3T3-E1 treated with β-PVDF-Mg patches, a transwell assay was performed (**Figure S5**). MC3T3-E1 in the β-PVDF-Mg and β-PVDF-Mg+US groups showed enhanced migration behavior compared to other groups (**Figure 5A**, **F**), demonstrating Mg^{2+} chemotactic effect. Also, cellular senescence has been implicated in impaired tissue regeneration by affecting cell proliferation, differentiation, and local inflammatory responses. Therefore, SA-β-gal staining was performed to evaluate senescence-associated β-galactosidase activity in MC3T3-E1. Cells treated with β-PVDF-Mg+US and β-PVDF group with linear topological pattern (named β-PVDF groups) exhibited reduced SA-β-gal-positive staining (**Figure 5B, G**), suggesting an attenuation of senescence-associated characteristics under the combined physical and chemical stimulation. Moreover, bone repair cannot be achieved without angiogenesis [64, 65]. It was observed that β-PVDF-Mg patches significantly accelerated HUVECs migration, and increased branch point counts (**Figure 5C, D, H, I, J**). This synergistic angiogenic promotion stems from combined chemical (Mg^{2+}) and physical stimulation modalities.

Excessive ROS can lead to cellular dysfunction [66]. To study whether β-PVDF-Mg patch could mitigate inflammation and maintain cellular homeostasis by inhibiting ROS production, we detected ROS levels. As shown in **Figure 5E**, **K**, under US stimulation, the β-PVDF-Mg containing Mg^{2+} group (i.e., β-PVDF-Mg+US group) exhibited lower ROS than the Mg^{2+}-free β-PVDF group (i.e., β-PVDF+US group), as Mg^{2+} has a definitive anti-ROS effect. Similarly, under identical control conditions, the β-PVDF-Mg group with US stimulation (i.e., β-PVDF-Mg+US group) exhibited lower ROS expression levels compared to the US-free β-PVDF-Mg group (β-PVDF-Mg group). One possible explanation for this finding is the piezoelectric effect effectively suppressing excessive ROS production by cells, thereby reducing cellular damage. Notably, β-PVDF patches with micro-nano linear topological structures (i.e., β-PVDF group) demonstrated comparable results to β-PVDF patches with smooth surface (i.e., Control group), indicating that the linear topological structure of β-PVDF independently mitigates oxidative stress. In conjunction with the experimental results of **Figure 5E**, **K**, among all experimental groups, the cells in the β-PVDF-Mg+US group produced the least ROS and the least oxidative damage. This finding suggests multiple synergistic antioxidant mechanisms. In detail, Mg^{2+} has been associated with cellular redox homeostasis, and reduced Mg availability can exacerbate ROS production and oxidative stress [67, 68]; piezoelectric effect synergistically amplified ROS inhibition; β-PVDF's linear topology independently attenuated oxidative stress, collectively establishing chemical (Mg^{2+}) and physical (piezoelectric effect, topology) antioxidant synergy.

Immunomodulatory and antimicrobial effects *in vitro* of the β-PVDF-Mg patches

Macrophage polarization studies were conducted to explore the immunomodulation of β-PVDF-Mg patches. Control experiments confirmed that lipopolysaccharide (LPS) stimulation induced M0-to-M1 polarization (pancake-like morphology), while IL-4/IL-13 triggered M2 polarization (elongated morphology), as evidenced by **Figure 6A**. Notably, β-PVDF patches with aligned topological patterns and US stimulation separately promoted comparable elongation in M0 cells to IL-4/IL-13-induced M2 polarization, as quantified by nuclear axis ratios (**Figure 6E**). M1-polarized macrophages exhibited

elevated iNOS expression, while M2 polarization was characterized by Arg-1 dominance (**Figure 6B**, **C**). Notably, β-PVDF variants with linear topology pattern and US stimulation reversed LPS-induced M1 polarization, significantly upregulating Arg-1 while suppressing iNOS (**Figure 6D**, **F**, **G**). In particular, β-PVDF-Mg+US and β-PVDF-Mg groups exhibited the higher Arg-1 and lower iNOS expression versus β-PVDF+US and β-PVDF groups, demonstrating positive effect of Mg^{2+} on M2 polarization. To further validate the macrophage phenotypic response, flow cytometric analysis of CD86 and CD206 was performed. The β-PVDF-Mg+US group exhibited a reduced proportion of CD86 positive macrophages (0.78%) and an increased proportion of CD206 positive macrophages (45.9%) (**Figure S6**). Among the experimental groups, β-PVDF-Mg+US showed the most pronounced shift toward a CD206-dominant phenotype. These flow-cytometric results were consistent with the increased Arg-1 and decreased iNOS signals observed by IF, providing additional evidence that the combined treatment favored a reparative macrophage phenotype. The results also suggested a contribution from the linear surface topography, whereas the difference between β-PVDF+US and β-PVDF-Mg+US suggested an additional contribution associated with Mg^{2+} incorporation/release. Furthermore, US treatment increased the reparative phenotypic response in the corresponding piezoelectric patch groups.

To evaluate preliminary *in vitro* antibacterial activity of β-PVDF-Mg patches under US stimulation, the bacteria were cultured on the patches and treated with US. The β-PVDF and β-PVDF-Mg exhibited comparable colony counts, suggesting that the piezoelectric material and Mg^{2+} did not have intrinsic antibacterial activities (**Figure S7A-B**). However, colony formation was significantly reduced in the β-PVDF+US and β-PVDF-Mg+US groups, whereas US alone did not alter colony counts (**Figure S7E-F**). So, the US-induced piezoelectric effect of β-PVDF can effectively inactivate bacteria, such as *S. aureus* and *E. coli*. In addition, the morphology of the bacteria treated with or without US stimulation was observed. **Figure S7C-D** revealed severe bacterial structural damage after β-PVDF-Mg+US treatment, whereas the largely preserved morphology observed in the β-PVDF-Mg group without US. According to previous studies, β-PVDF can generate transient electric fields or charges on its surface by piezoelectric effect. Previous studies have suggested that piezoelectric surface charges may perturb bacterial membrane integrity through electrostatic interactions. Consistent with this possibility, SEM images in the present study showed morphological disruption after β-PVDF-Mg+US treatment. However, the precise antibacterial mechanism was not directly investigated here. Although the β-PVDF-Mg patch exhibited antibacterial activity, the present study did not evaluate its therapeutic efficacy in an infected bone defect model. The results should serve as preliminary evidence for the material's potential to reduce infection risk. Future studies using clinically relevant infected bone defect models will be served to evaluate whether the *in vitro* antibacterial effects can be translated into therapeutic benefits *in vivo*.

The β-PVDF-Mg patches demonstrate osteogenic effects *in vivo*

Quantitative micro-CT analysis confirmed superior osseous regeneration in the β-PVDF-Mg+US group, which exhibited the most favorable values across the predefined structural indices. Improvements were also detected in groups receiving either topographical or piezoelectric cues alone, although these effects were less pronounced than those observed with the combined treatment (**Figure 7A-E**). Interestingly, the Control+US group and the β-PVDF group with linear topology had a higher BMD, BV/TV and BS/TS. These may be attributed to piezoelectric effect and topology pattern inducing osteogenesis [69-71]. In addition, the β-PVDF-Mg+US group showed the highest levels of bone morphogenetic protein 2 (BMP-2)/OCN/OPN by the quantitative analysis (**Figure 7F-H**). Therefore, the US-triggered β-PVDF-Mg patch exhibited the optimal osteogenesis capacity. Interpretation of the *in vivo* data is limited by the small sample size (n = 4 per group) and assessment at only one time point (8 weeks). Sensitivity analysis indicated that the present design had approximately 80% power to detect large overall treatment effects (Cohen's $f \approx 0.85$), but it may have been insufficiently powered to detect moderate or small between-group differences. Thus, nonsignificant differences should not be regarded as demonstrating equivalence among the treatment groups. Future studies with larger, prospectively powered cohorts and multiple longitudinal time points are warranted to further evaluate the robustness and temporal evolution of the treatment effects.

Among the treatment groups, β-PVDF-Mg+US produced the most extensive tissue filling and new bone, accompanied by increased collagen deposition and stronger expression of osteogenic markers (**Figure 8A**). Meanwhile, the collagen deposition was greatest in the β-PVDF-Mg+US, suggesting that the β-PVDF-Mg with US stimulation could enhance bone regeneration (**Figure 8B, D**). Interestingly, the Control+US group and the β-PVDF group with linear topology had more bone formation, thicker new bone,

and greater collagen deposition (**Figure 8A, B and D**). These may be attributed to piezoelectric effect and topology pattern inducing osteogenesis [69, 71]. Besides, the number of blood vessels can reflect the quality of bone repair. The Control+US group and the β-PVDF group with linear topology had higher CD31-positive vascular density. This increase may be due to the pro-vascularization of piezoelectric effect and topology pattern. The β-PVDF-Mg+US group exhibited enhanced vascular-related signals during bone repair. Interestingly, the CD31-positive area showed a reduction at the late implantation stage, which may reflect changes in angiogenic dynamics during the progression from vascular formation to tissue remodeling (**Figure 8C, E**). This interpretation should be validated further using analyses specifically addressing vascular maturation.

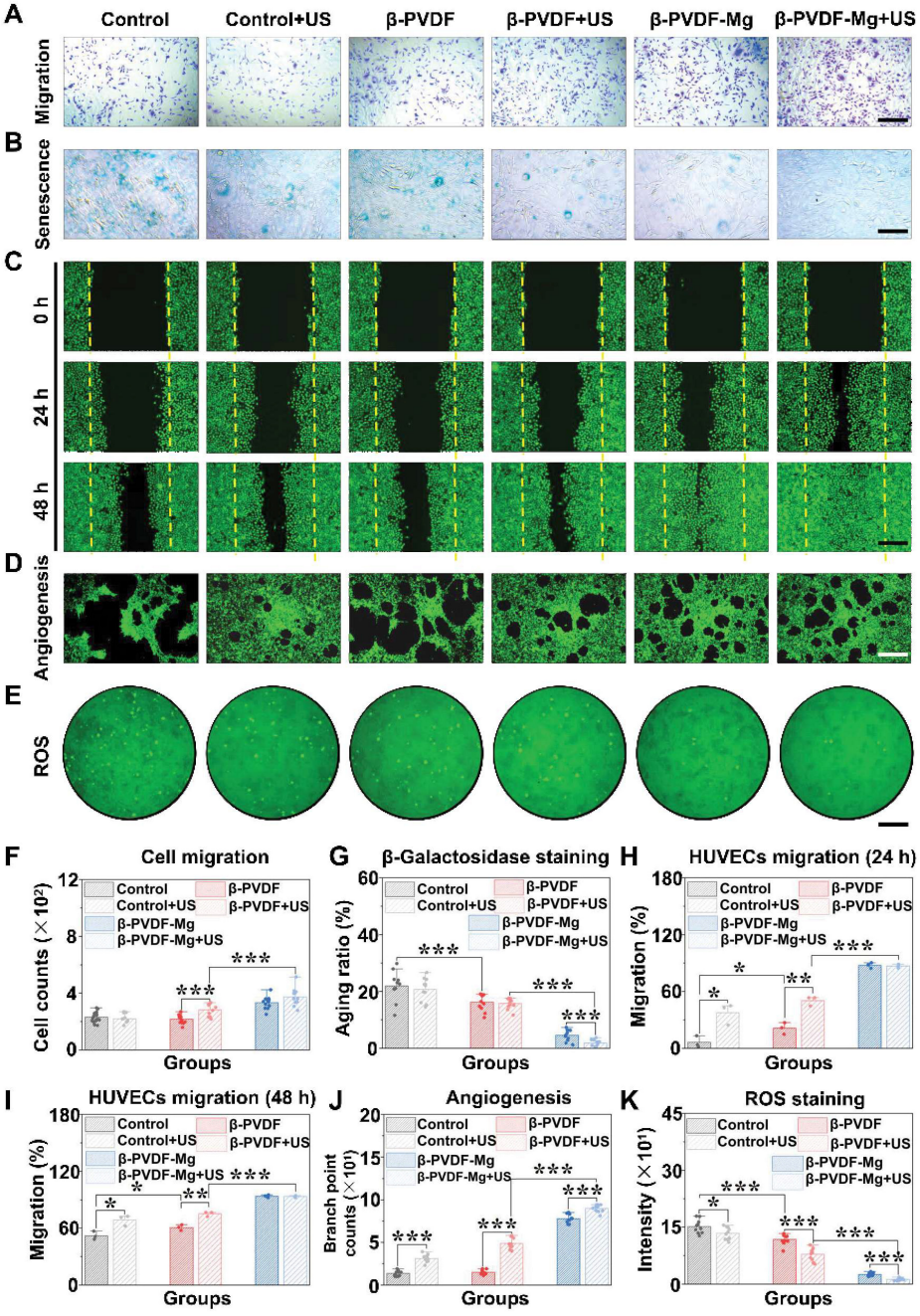


Figure 5. The β-PVDF-Mg patches promote cell homing and angiogenesis, enhance antioxidant activity, and attenuate senescence-associated phenotype in osteogenic cells. (A) Transwell assay using MC3T3-E1 after 24 h culture; scale bar: 100 μm. **(B)** Senescence-Associated β-Galactosidase (SA-β-Gal) staining; scale bar: 50 μm. **(C)** Migration assay of HUVECs cultured in different groups at specific time points (n = 3); scale bar: 100 μm. **(D)** Matrigel angiogenesis assay using HUVECs cultured for 48 h; scale bar: 100 μm. **(E)** ROS staining of RAW264.7 cells; scale bar: 100 μm. **(F-K)** Statistical analysis of cell migration **(F)**, SA-β-Gal staining **(G)**, 24 h HUVECs migration ratio **(H)**, 48 h HUVECs migration ratio **(I)**, branch point counts of vessel **(J)** and R OS staining **(K)** based on fluorescent images. Data are mean ± SD from at least three biologically independent replicates; one-way ANOVA: *$p < 0.05$, **$p < 0.01$, ***$p < 0.001$.

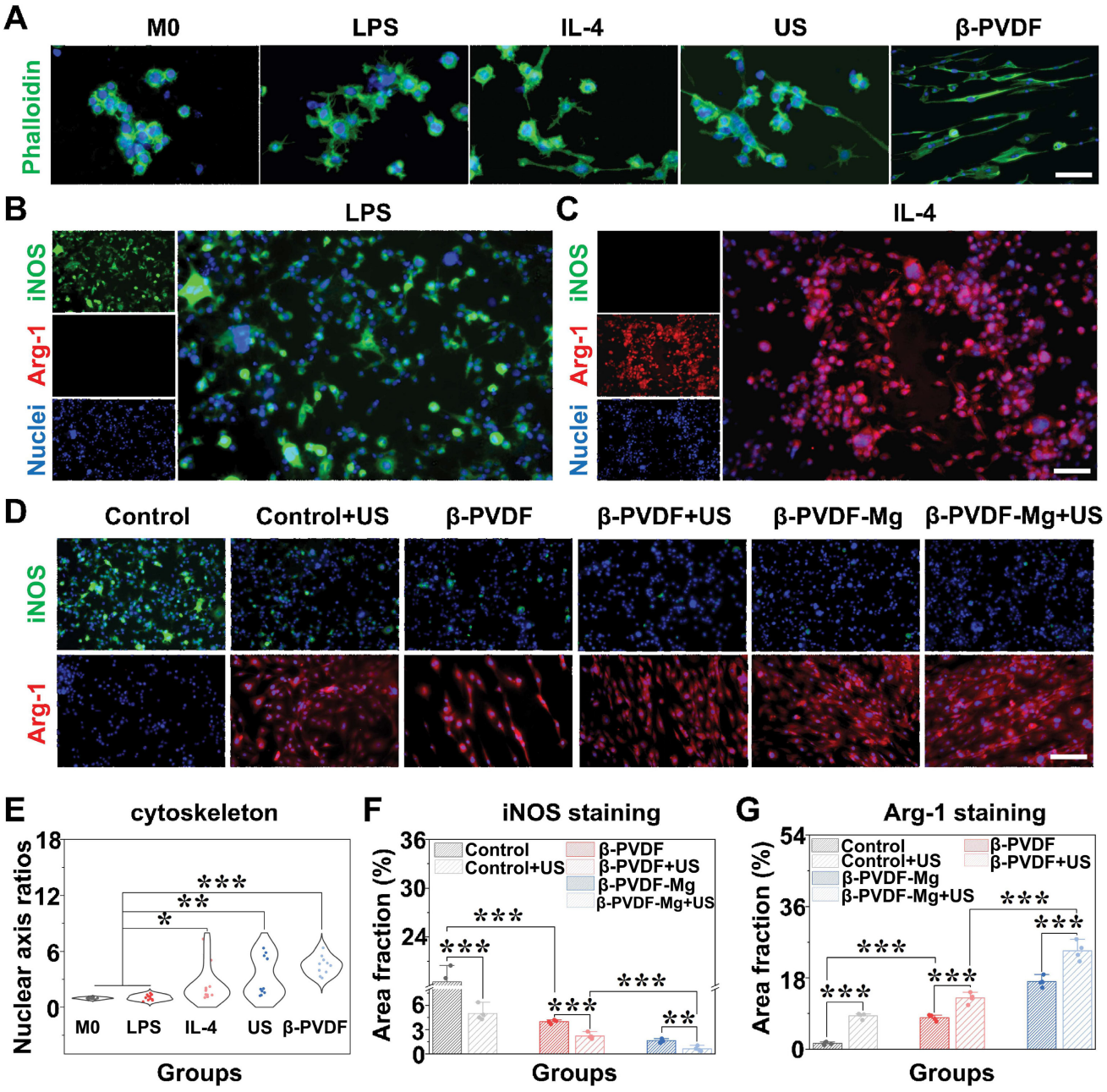


Figure 6. The β-PVDF-Mg patches promote M2 polarization and inhibit M1 polarization in RAW264.7. (A) RAW264.7 cytoskeleton staining *in vitro*: representative images of RAW264.7 cytoskeleton stained with phalloidin (48 h) (n = 4); scale bar: 20 μm. **(B-D)** IF staining of iNOS (an M1 marker) and Arg-1 (an M2 marker) after 3 days of culture (n = 4); the scale bars represent 80 μm and 20 μm, separately. **(E-G)** Statistical analysis of RAW264.7 nuclear axis ratios **(E)**, iNOS **(F)** and Arg-1 **(G)** fluorescence intensity by ImageJ software. Data are mean ± SD from four biologically independent replicates; one-way ANOVA: *$p < 0.05$, **$p < 0.01$, ***$p < 0.001$.

SOD1 can inhibit ROS damage during bone repair. It was found that the β-PVDF-Mg and β-PVDF-Mg+US groups exhibited elevated levels of SOD1 expression, indicating the reduced oxidative damage during the late-stage bone remodeling process via the Mg^{2+}-driven antioxidant response (**Figure S8A, B**). Additionally, the piezoelectric effect of β-PVDF-Mg+US resulted in maximal induction of OCN and OPN expression, thereby suggesting the enhanced osteoblast activity and accelerated biomineralization (**Figure 9A, C**). These results could be attributed to the Mg^{2+}-mediated osteoanabolic effects, including suppressing bone resorption and enhancing mineralization-associated protein secretion, and thus, achieving biomimetic coupling of osteogenic differentiation and matrix maturation [57, 58]. Concurrently, β-PVDF with a linear topology pattern independently upregulated osteogenic markers by priming osteoblast through topographical cues. Additionally, the Control+US group expressed more OCN and OPN, likely due to the osteogenic effects of US. These findings establish synergistic interplay

between physical cues (piezoelectric effect, topology pattern) and chemical cues (Mg^{2+}), resulting in comprehensive osteogenic enhancement.

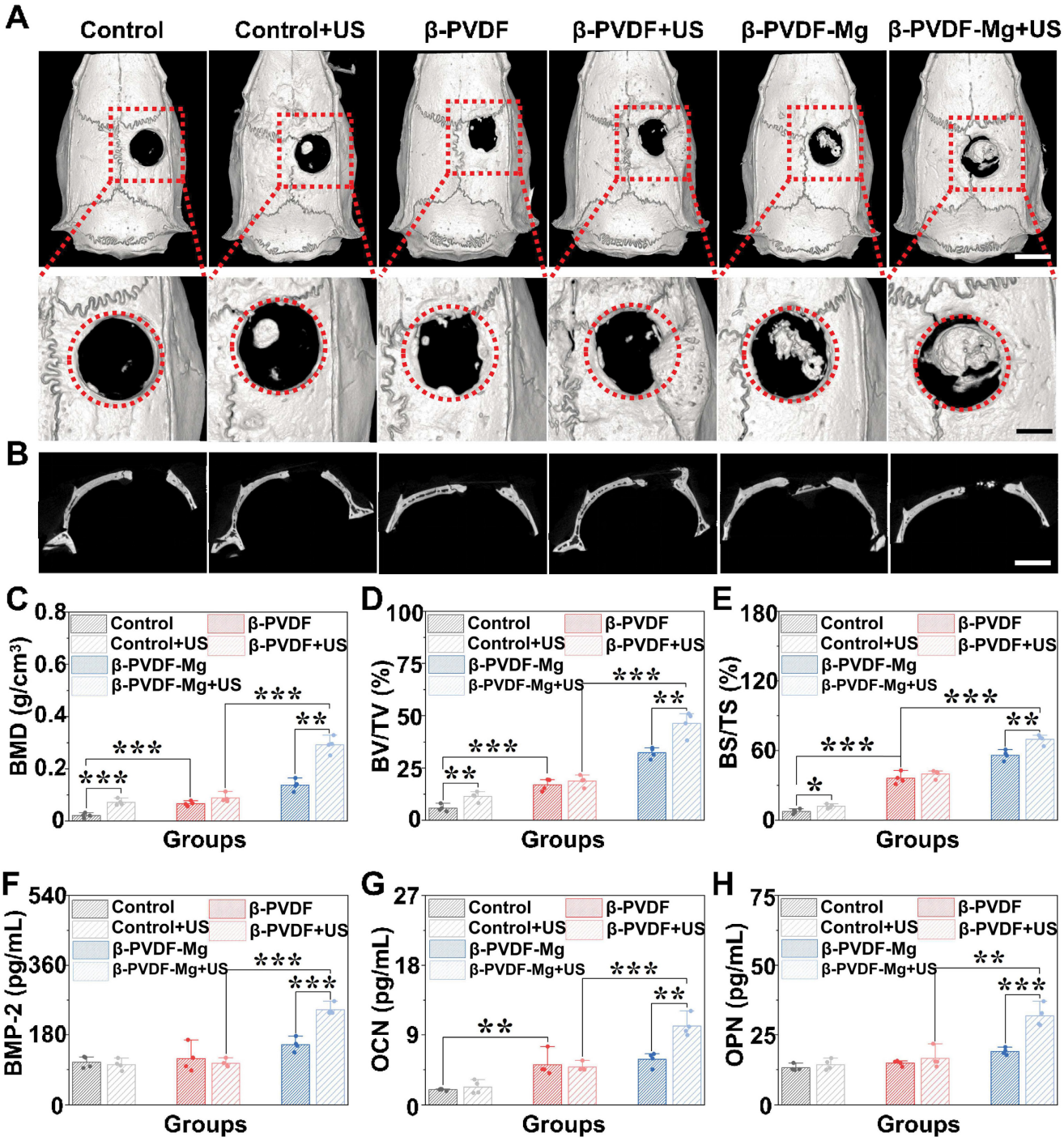


Figure 7. Micro-CT evaluation of calvarial regeneration after 8 weeks. (A, B) Three-dimensional reconstructions and corresponding sectional images showing defect closure in each group (n = 4). Original defect boundaries are indicated by red circles; scale bars: 4 mm (**A**) and 2.5 mm (**B**). **(C–E)** Quantitative comparison of BMD, BV/TV, and BS/TS within the predefined defect region. **(F–H)** Serum levels of osteogenesis-related proteins determined by ELISA (n = 4). Data are mean ± SD from four biologically independent replicates; one-way ANOVA: *$p < 0.05$, **$p < 0.01$, ***$p < 0.001$.

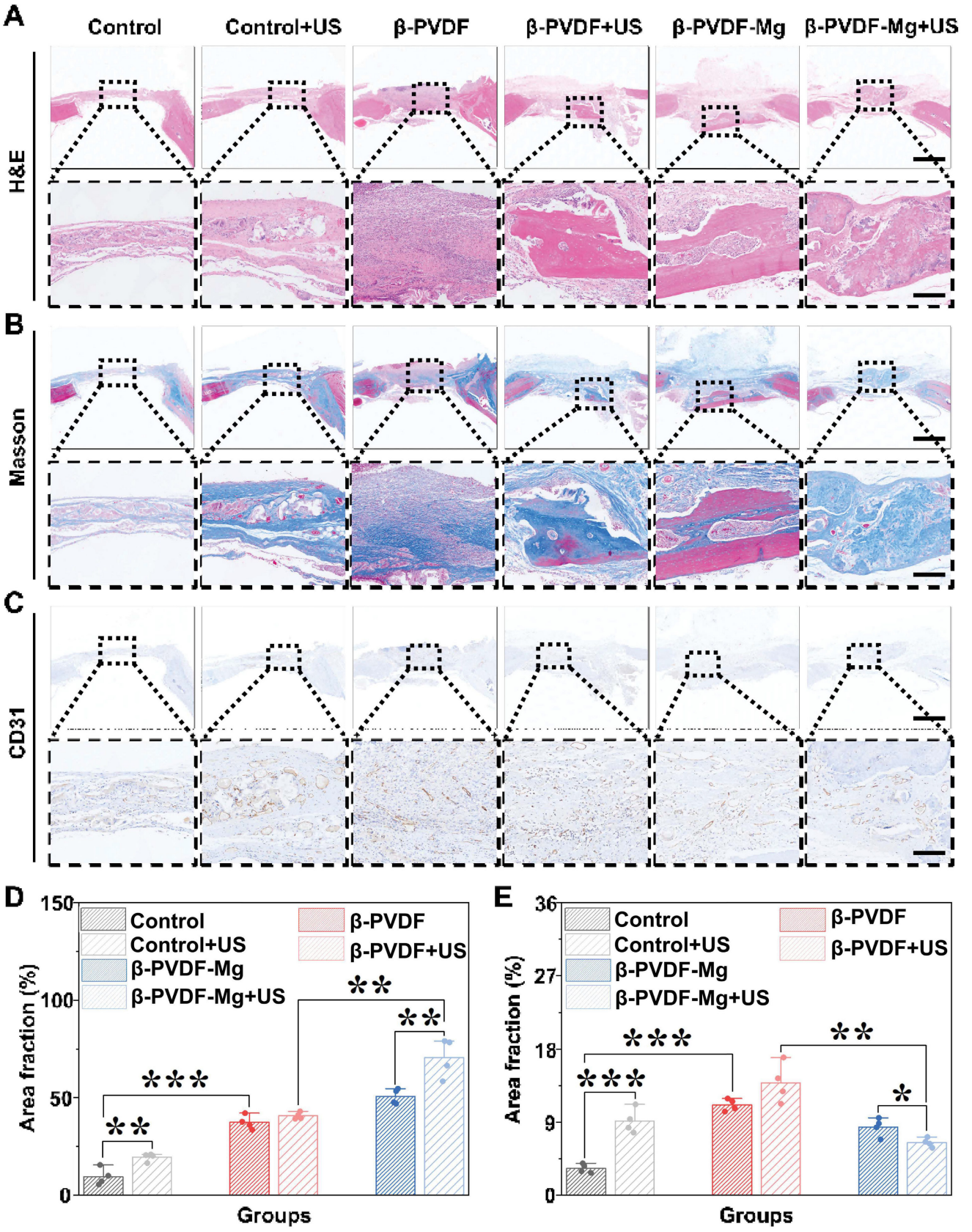


Figure 8. The β-PVDF-Mg patches promote osteogenesis and angiogenesis *in vivo*. (A) H&E staining of bone after 8 weeks treatments; scale bars: 1.5 mm (top) and 100 μm (bottom). **(B)** Masson staining collagen after 8 weeks treatments; scale bars: 1.5 mm (top) and 100 μm (bottom). **(C)** IHC staining of CD31; scale bars: 1.5 mm (top) and 50 μm (bottom). **(D, E)** Statistical analysis of collagen **(D)** and CD31 **(E)** (n = 4). (Dashed boxes indicate the regions selected for the corresponding high-magnification views; equivalent anatomical regions within the original defect area were selected across all six groups, with identical magnification settings and the dimensions and positions of the dashed regions of interest standardized as much as possible within each staining panel.) Data are mean ± SD from four biologically independent replicates; one-way ANOVA: **p* < 0.05, ***p* < 0.01, ****p* < 0.001.

Immunomodulatory effects of the β-PVDF-Mg patches during bone repair

M1 macrophages orchestrate the clearance of early-stage tissue damage, but if unregulated, they risk exacerbating inflammation [72]. In contrast, M2 polarization dominates regenerative phases via anti-inflammatory and pro-angiogenic processes, thereby facilitating bone repair [73]. The tissues treated with β-PVDF-Mg patches exhibited upregulated Arg-1 and downregulated iNOS polarization dominance in defect sites, and the effects were better with US stimulation (**Figure 9B and D**). So, the Mg^{2+} can modulate macrophage phenotype and osteoimmune signaling in a concentration- and stage-dependent manner, thereby influencing bone regeneration [74, 75], and it was enhanced by the US-enhanced immunometabolic reprogramming [76]. Interestingly, both the Control+US group and the β-PVDF group with linear topology had higher Arg-1 and lower iNOS expression, suggesting that the piezoelectric effect and topology pattern promote M2 polarization while suppressing M1 activation [77]. Together, these findings suggest that Mg^{2+} and physical cues, including surface topography and US-responsive piezoelectric stimulation, cooperatively modulate macrophage phenotype and contribute to a pro-regenerative osteoimmune microenvironment [75-77]. As the primary shapers of the early inflammatory microenvironment, macrophages serve as the core cellular target of this integrated mechanism. Our data showed that the β-PVDF-Mg+US group can drive macrophage M2 polarization (high Arg-1, low iNOS; **Figure 6**), highlighting the synergistic action between piezoelectric effect and Mg^{2+} release. We have confirmed that the amount of Mg^{2+} release directly correlates with the piezoelectric voltage output of the patch, indicating that the piezoelectric effect is the primary physical mechanism regulating ion release. These synergistic signals may be integrated as follows: piezoelectric microcurrents may modulate membrane potential and calcium influx, potentially enhancing cellular sensitivity to or uptake of Mg^{2+} from the microenvironment; meanwhile, intracellular Mg^{2+}, acting as a critical signaling cofactor, may amplify the biological effects of downstream pathways. For instance, Mg^{2+} is an essential cofactor for ATP, directly powering cellular activities. Mg^{2+} and US-responsive piezoelectric stimulation may influence signaling networks including PI3K-AKT and MAPK-ERK, as suggested by the transcriptomic enrichment and phosphorylation data obtained in this study (**Figure 10**). *RUNX2* acts as the "master switch" for osteogenic differentiation, driving the expression of downstream osteogenic gene clusters (*Col-I*, *ALP*, *OPN*). Beyond directly stimulating osteogenesis, Mg^{2+} can induce various cells, including macrophages, to secrete critical factors like vascular endothelial growth factor (VEGF). It can also directly act on endothelial cells, promoting their migration, proliferation, and tubulogenesis, thereby establishing the essential blood supply for new bone tissue [3, 4]. By consuming the substrate L-arginine, it competitively inhibits the pro-inflammatory pathway mediated by inducible iNOS, while generating products such as proline, which promote collagen synthesis and tissue repair. The pro-regenerative microenvironment mediated by the activated M2 macrophages functions as a switch initiating functional repair: by establishing an anti-inflammatory, pro-angiogenic, and pro-osteogenic microenvironment, they systematically steer the early inflammatory response toward functional tissue regeneration [78-82]. Therefore, the US-triggered piezoelectric output can synergize with Mg^{2+} to enhance osteogenesis, angiogenesis, and immunomodulation, forming a coordinated pro-regenerative cascade. The surface topology continues to provide an optimal scaffold for osteoblast attachment and spreading during this phase. To preliminarily evaluate systemic biocompatibility during the 8-week implantation period, H&E staining of various organs was performed. All treatment groups exhibited normal tissue structure and morphology (**Figure S9**), indicating that β-PVDF-Mg patch exhibits biocompatibility *in vivo* within the investigated 8-week period. Because PVDF is a chemically stable and non-degradable polymer, the current 8-week implantation study primarily demonstrates short-term systemic compatibility. Although the structural persistence and piezoelectric stability of PVDF support sustained regenerative stimulation, its long-term fate requires further investigation, particularly with respect to foreign-body reactions, fibrous encapsulation, and post-repair implant management. Further studies should include longer implantation durations (≥12 weeks), which is essential before clinical translation of the β-PVDF-Mg platform can be considered.

To further evaluate Mg^{2+} release during long-term implantation, the residual Mg content of β-PVDF-Mg patches retrieved after 8 weeks was quantified by ICP-MS. Compared with the initial patches (Mg^{2+}: 0.05 mmol), a substantial reduction in residual Mg^{2+} was observed after implantation. Moreover, patches subjected to repeated US stimulation exhibited a lower residual Mg^{2+} content (Mg^{2+}: 0.004 mmol) than those without US treatment (Mg^{2+}: 0.041 mmol) (**Table S5**), supporting the ability of US stimulation to facilitate Mg^{2+} release *in vivo*. The pattern of residual Mg detected *in vivo* was in

agreement with the release profile obtained from the multi-cycle *in vitro* study. Starting from an initial loading of 0.05 mmol Mg per patch, 0.004 mmol remained in the β-PVDF-Mg+US group after 8 weeks, corresponding to an approximate cumulative release of 92%, whereas 0.041 mmol remained in the non-US group, corresponding to approximately 18% release. The pronounced US-dependent enhancement therefore closely paralleled the high cumulative release observed *in vitro*. Nevertheless, the *in vivo* and *in vitro* release fractions were not identical, likely reflecting differences between controlled PBS conditions and the dynamic tissue environment. Notably, the residual-patch analysis reflects Mg depletion from the implant rather than a complete *in vivo* Mg mass balance. The released Mg^{2+} may undergo local tissue retention, extracellular-matrix association, cellular uptake, incorporation into newly mineralizing tissue, vascular transport, and systemic clearance. Because local tissue, serum, urinary, and organ Mg levels were not directly quantified, the relative contributions of local accumulation and systemic clearance cannot be determined.

In addition, temperature generated by US monitoring was performed (1.5 MHz, 30 mW/cm², 20% duty cycle, 20 min). The temperature of the sample environment was monitored throughout US exposure and compared with the corresponding sham-treated condition (no US). No appreciable bulk temperature increase was observed during the 20 min LIPUS exposure in both *in vivo* and *in vitro* (**Figure S10**), suggesting that the observed biological effects were unlikely to be primarily attributable to US-induced heating.

Proposed hypothetical model of β-PVDF-Mg+US-mediated osteoimmune regulation

To further test the immunoregulation mechanisms of the β-PVDF-Mg patches under US stimulation, RNA sequencing analysis of macrophages treated by β-PVDF-Mg patches was performed. 1,112 differentially expressed genes (*DEGs*) in macrophages (267 upregulated; 845 downregulated) in the β-PVDF-Mg+US group versus the Control group was revealed (**Figure 10A**). Cluster diagram analysis identified the raise of functionally distinct genes in the β-PVDF-Mg+US group (**Figure 10B**), including *Igf1*, associated with regenerative growth-factor signaling [83]; *Dusp5*, regulating MAPK signaling through dephosphorylation of ERK [84]; *Il1rn*, regulating *IL-1*-mediated inflammatory signaling [85]; *Col5a3* and *P3h2* related to extracellular-matrix organization [86] and collagen modification [87], respectively. These expression changes were further verified by RT-qPCR (**Figure 10C**). Collectively, these *DEGs* are associated with growth-factor signaling, inflammatory regulation, MAPK regulation, and extracellular-matrix organization/remodeling. In addition, kyoto encyclopedia of genes and genomes (KEGG) enrichment analysis identified the PI3K-AKT and MAPK signaling pathways among the significantly enriched pathways associated with β-PVDF-Mg+US treatment, suggesting their potential involvement in the macrophage response. (**Figure 10D**). The PI3K-AKT axis coordinates the inflammation-repair balance by dual osteoblast activation and collagen deposition, as well as RANKL-mediated osteoclast suppression, and thus, maintaining the bone metabolic homeostasis [88, 89]. The observed increase in AKT and ERK phosphorylation is consistent with the involvement of these signaling pathways in macrophage regulation [90, 91].

Biological processes showed significant immune response pathway enrichment (**Figure 10E**), while cellular components and molecular functions predominantly featured integrin-receptor complexes through Gene Ontology (GO) analysis. These transcriptomic results indicated that β-PVDF-Mg+US treatment is related to coordinated changes in immune- and regeneration-related signaling networks in macrophages. Moreover, the PPI analysis identifies that the core hub genes (*Igf1*, *Spp1*, *IL1a*, *IL1b*, *Ccl5*) that form a tightly interacting network, outlining a macrophage-mediated, immune-regulated pro-regenerative model. These results suggest that the β-PVDF-Mg patches modulate the activation state and secretion profile of macrophages (M1, M2). On one hand, the altered expression of *Il1a*, *Il1b* and *Ccl5* is consistent with an early macrophage-associated inflammatory and cell-recruitment response during bone healing [75]; on the other hand, they promote the transcription of key bone-contributing factors (e.g., macrophage M2-originated *Igf1*) and immune-osteoconjugate molecules (e.g., *Spp1*) [92, 93]. Meanwhile, negative feedback regulatory mechanisms built into the network (e.g., *Il1rn* antagonizing *IL1* signaling) suggest that the β-PVDF-Mg patch promotes the timely abatement of inflammation and the establishment of immune homeostasis. Ultimately, macrophage-derived signals, particularly Igf1, may contribute to bone regeneration by supporting Runx2-associated osteoblast differentiation [94], while Nfatc1 and Acp5 are more closely associated with osteoclast differentiation and bone remodeling (**Figure 10F**) [95, 96].

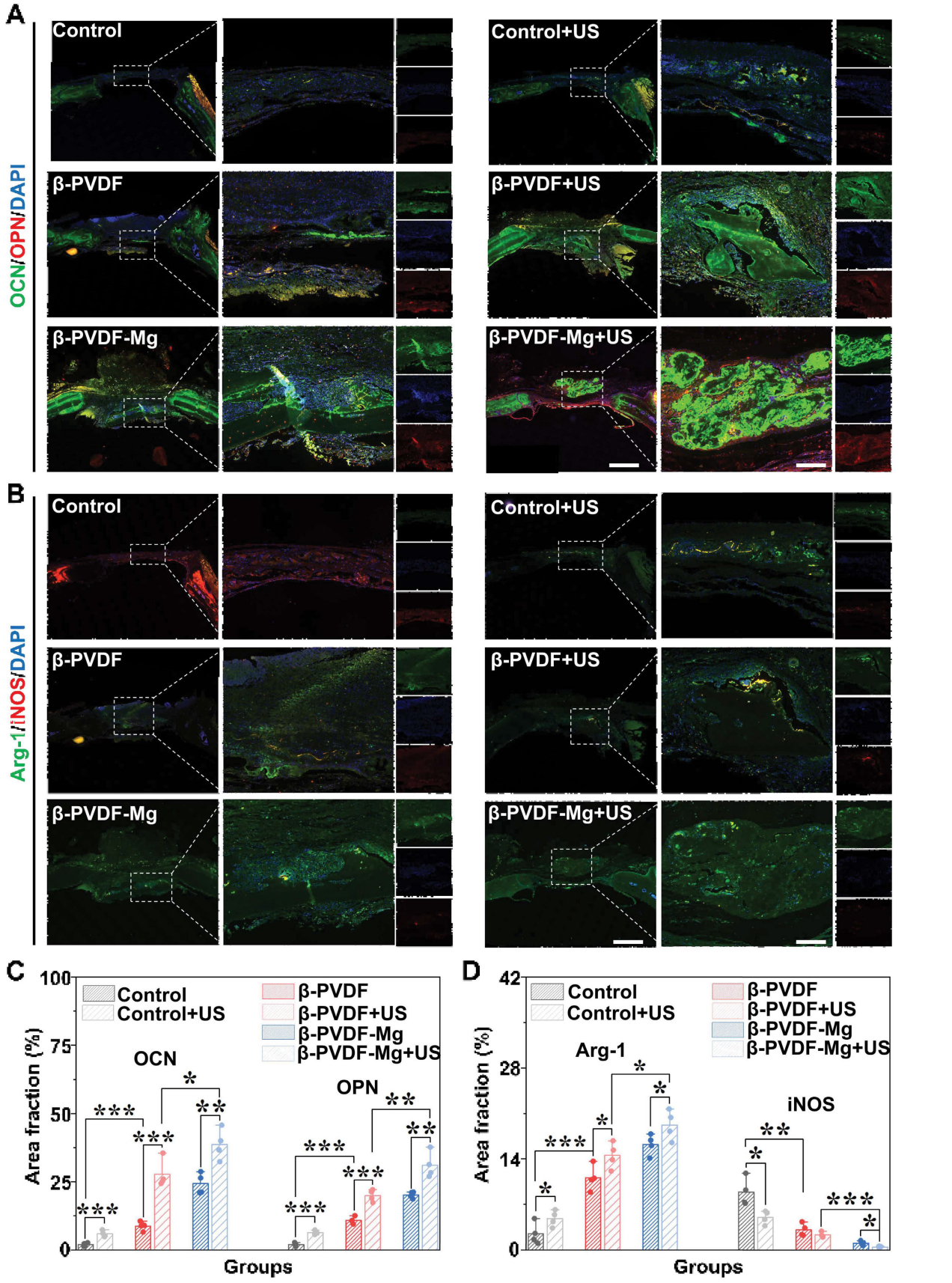


Figure 9. The β-PVDF-Mg patches promote osteogenesis and immunomodulation *in vivo*. (A-B) Representative IF staining after 8 weeks treatments; scale bars: 1.5 mm (left) and 100 μm (right). **(C, D)** Statistical analysis of relevant marker (n = 4). Data are mean ± SD from four biologically independent replicates; one-way ANOVA: **p* < 0.05, ***p* < 0.01, ****p* < 0.001.

Phosphorylation-specific ELISA further supported the transcriptomic findings, with the p-AKT/AKT and p-ERK/ERK ratios increasing from 0.996 ± 0.027 and 1.002 ± 0.019 in the Control group to 1.481 ± 0.062 and 2.176 ± 0.218 in the β-PVDF-Mg+US group, respectively (**Figure S11**). Collectively, the transcriptomic enrichment and phosphorylation-level analyses indicate that β-PVDF-Mg+US treatment is related to enhanced PI3K-AKT- and MAPK-ERK-related signaling in macrophages. These signaling changes may promote the reparative macrophage phenotype. The relationships summarized in **Figure 10G** should be regarded as a conceptual mechanistic scheme based on the current findings.

To further determine whether PI3K-AKT and MAPK-ERK signaling functionally contributed to the macrophage response, pharmacological inhibition experiments were performed using LY294002 and U0126 (**Figure S12, S13**). The β-PVDF-Mg+US group increased p-AKT and p-ERK fluorescence, consistent with the phosphorylation-specific ELISA results. LY294002 treatment significantly reduced p-AKT signaling, whereas U0126 markedly suppressed p-ERK signaling, confirming effective inhibition of the respective pathways. Importantly, β-PVDF-Mg+US treatment markedly increased Arg-1 expression, indicating a reparative M2-like macrophage phenotype, whereas inhibition of either PI3K-AKT with LY294002 or MAPK-ERK with U0126 significantly reduced Arg-1 expression (**Figures S12A, C and S13A, C**), supporting the functional involvement of both signaling pathways in β-PVDF-Mg+US-mediated macrophage polarization.

We next investigated whether pathway-dependent macrophage regulation contributed to downstream osteogenic paracrine effects. MC3T3-E1 cultured with conditioned medium from β-PVDF-Mg+US-treated macrophages exhibited markedly increased RUNX2 and OPN expression compared with cells exposed to control macrophage-conditioned medium. In contrast, conditioned media derived from macrophages treated with β-PVDF-Mg+US + LY294002 or β-PVDF-Mg+US + U0126 resulted in significantly lower RUNX2 and OPN expression than conditioned medium from the β-PVDF-Mg+US group (**Figure S12B, D and S13B, D**). So, the inhibition of either PI3K-AKT or MAPK-ERK signaling in macrophages attenuated the pro-osteogenic activity of their conditioned medium. Overall, these results verify a functional link between PI3K-AKT- and MAPK-ERK-associated macrophage regulation and the downstream pro-osteogenic paracrine response induced by β-PVDF-Mg under US stimulation.

Emerging studies have shown that piezoelectric cues and bioactive ion delivery can be incorporated into a unified platform for bone regeneration, enabling coordinated physical and biochemical regulation. Our β-PVDF-Mg patch differs from biodegradable piezoelectric scaffolds (relying on loading/degradation) and other LIPUS-activated systems (lacking Mg/topography) by using external US to simultaneously regulate piezoelectric stimulation and Mg^{2+} release while preserving sustained topography. Unlike NIR-based sequential systems, we achieve coordinated control via a single LIPUS input, albeit without stage-specific switching. Animal experiments confirmed that the β-PVDF-Mg+US group exhibited optimal osteogenic outcomes, including BMD, BV/TV and collagen deposition, highlighting the system's significant bone repair efficacy.

The comparative group design provides partial separation of the three functional cues incorporated in the present platform. First, comparison between smooth control and topographical β-PVDF patches demonstrates the contribution associated with the micro-nano linear surface structure. The patterned surface promoted cell alignment and was accompanied by enhanced osteogenic and reparative macrophage-associated responses, supporting a persistent contact-guidance role of the topography. Second, comparison of β-PVDF with β-PVDF+US demonstrates the additional biological response associated with US activation. The US-treated group showed enhanced osteogenic and immunomodulatory outcomes, consistent with an additional dynamic electromechanical stimulus. Because US itself may also exert direct mechanical effects on cells, however, this comparison should be interpreted as an US-associated piezoelectric activation effect, rather than as an exclusively electrical microcurrent effect. Third, comparison of β-PVDF with β-PVDF-Mg, and β-PVDF+US with β-PVDF-Mg+US, demonstrates the additional contribution associated with Mg incorporation. Mg-containing patches enhanced several osteogenic, angiogenic, and reparative macrophage-associated outcomes, supporting a biochemical contribution of Mg^{2+} availability. Together, these elements form "Physical and Chemical Factors-Immunity-Bone" regulatory network. US triggers piezoelectric output and controls Mg^{2+} release kinetics, while the topological pattern provides sustained contact guidance.

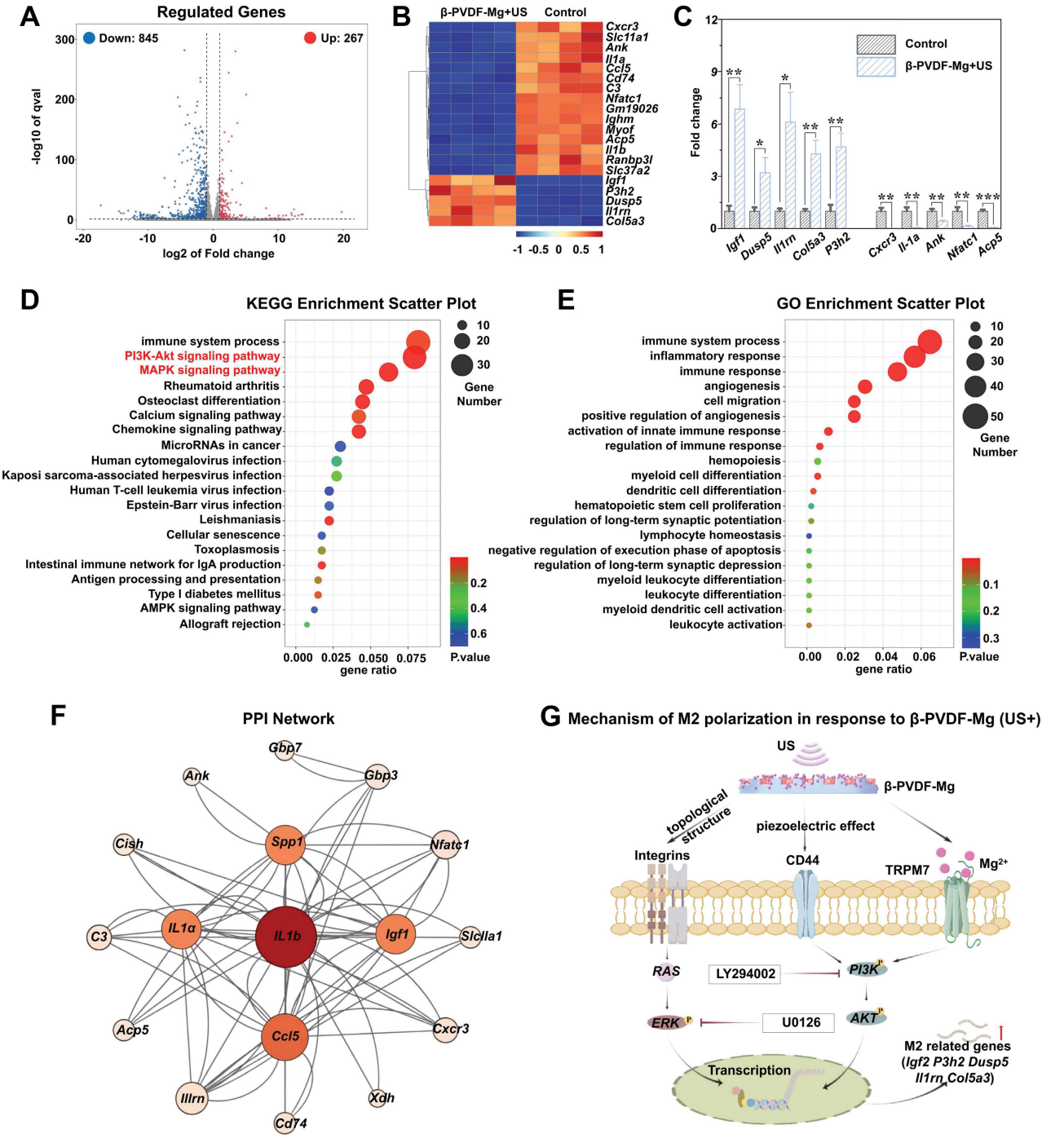


Figure 10. Transcriptomic, phosphorylation, and functional analyses of β-PVDF-Mg+US-mediated osteoimmune regulation. (A) Differentially expressed transcripts visualized by volcano analysis. **(B)** Hierarchical clustering of genes altered between β-PVDF-Mg+US and Control. **(C)** RT-qPCR validation of selected targets (n = 3). **(D, E)** The analysis of KEGG and GO. **(F)** The PPI network. **(G)** Mechanistic model illustrating the functional involvement of PI3K-AKT- and MAPK-ERK-associated signaling in β-PVDF-Mg+US-mediated macrophage regulation and downstream osteogenic responses, supported by transcriptomic, phosphorylation, and pharmacological inhibition analyses. Data are mean ± SD from three biologically independent replicates; one-way ANOVA: *$p < 0.05$, **$p < 0.01$, ***$p < 0.001$.

Macrophage responses to biomaterials are influenced by their chemical composition and their physical and structural characteristics. As summarized by Chen et al., multiple biomaterial properties, including surface structure, roughness, stiffness, pore architecture, and chemical composition, can influence macrophage phenotype and consequently affect bone regeneration [97]. In the present system, regulation of the osteoimmune microenvironment is integrated through three functionally coupled cues. First, the micro-nano linear topography provides a persistent physical cue at the cell-material interface. Second, US activation of the β-PVDF matrix generates a dynamic piezoelectric signal,

providing an additional electromechanical cue to cells. Third, Mg^{2+} incorporated within the patch provides a biochemical signal, while its release is enhanced by US activation of the piezoelectric system. Thus, rather than acting as three completely independent factors, surface topography, piezoelectric stimulation, and Mg^{2+} release constitute a coupled physical-electrical-chemical microenvironment. The present results showed that the patch supports a shift toward a reparative macrophage phenotype under the combined β-PVDF-Mg+US treatment. Such macrophage modulation may subsequently contribute to a local environment favorable for inflammation resolution, angiogenic responses, and osteogenic differentiation. This coordinated mechanism significantly accelerated bone defect healing in animal models, offering a novel strategy for designing smart bone repair materials with combined immunomodulatory and osteogenic functions.

Conclusions

The multimodal patch provides a US-responsive platform that integrates piezoelectric stimulation, Mg^{2+} release, and topographical guidance to promote a regenerative osteoimmune microenvironment, with PI3K-AKT and MAPK-ERK signaling functionally contributing to macrophage regulation and downstream osteogenic paracrine effects.

Abbreviations

Mg^{2+}: magnesium ion; PVDF: Poly(vinylidene fluoride); DMF: dimethylformamide; $MgCl_2{\cdot}6H_2O$: magnesium chloride hexahydrate; LSCM: laser scanning confocal microscopy; SEM: scanning electron microscopy; EDS: energy dispersive spectroscopy; XRD: X-ray diffraction; ATR: attenuated total reflection; FTIR: Fourier transform infrared spectroscopy; US: ultrasound; P-E: polarization-electric; WCA: water contact angle; DCFH-DA: 2′, 7′-dichlorodihydrofluorescein diacetate; Mg^{2+}: magnesium ion; PVDF: polyvinylidene fluoride; ICP-MS: Inductively coupled plasma-mass spectrometry; MC3T3-E1: mouse embryo osteoblast precursor cells; α-MEM medium: minimum essential medium α; DMEM: dulbecco's modified eagle medium; CCK-8: cell counting kit-8; BSA: bovine serum albumin; ALP: alkaline phosphatase; ARS: alizarin red s; BMNs: bone mineralization nodules; OCN: osteocalcin; OPN: osteopontin; Col-I: collagen type I; RT-qPCR: reverse transcription-qPCR; GAPDH: glyceraldehyde-3-phosphate dehydrogenase; PFA: paraformaldehyde; PBS: phosphate buffered saline; RUNX2: runt-related transcription factor 2; HUVECs: human umbilical vein endothelial cells; ROS: reactive oxygen species; LPS: lipopolysaccharide; iNOS: nitric oxide synthase; Arg-1: arginase-1; BMD: bone mineral density; BV/TV: bone volume/tissue volume; BS/TS: bone surface/tissue surface; H&E: hematoxylin and eosin; SOD1: superoxide dismutase 1; VEGF: vascular endothelial growth factor; DEGs: differentially expressed genes; KEGG: kyoto encyclopedia of genes and genomes; GO: Gene Ontology; ANOVA: analysis of variance; ELISA: enzyme-linked immunosorbent assay; IF: immunofluorescence; IHC: immuno-histochemistry; PLLA: poly(L-lactic acid); PHBV: poly(3-hydroxybutyrate-co-3-hydroxyvalerate); RNA: ribonucleic acid; ddH_2O: double distilled H_2O; ROI: regions of interest; LIPUS: low-intensity pulsed ultrasound; BMP-2: bone morphogenetic protein 2.

Supplementary Material

Supplementary figures and tables.
https://www.thno.org/v17p0818s1.pdf

Acknowledgments

Funding

The Jiangsu Province Frontier Technology Research and Development Program grant BF2024044; the National Key Research and Development Program Project grant 2023YFB3810204, 2020YFA0908200; the National Natural Science Foundation of China grant 82102335, 52403189.

Declaration of AI-assisted language editing

ChatGPT (OpenAI) was employed exclusively for language refinement during manuscript preparation. All AI-assisted content was subsequently reviewed and revised by the authors, who take full responsibility for the final manuscript.

Authorship contribution statement

Y. J. Zhao and Y. X. Wang designed the program; Z. W. Liu carried out the experiments; and Z. W. Liu, H. Zhang and Y. Wang wrote the paper.

Data availability

All experimental data generated in this work are available within the main manuscript (**Figure 1–10**), Supplementary information (Supplementary **Figure S1–S13** and Supplementary **Table S1-S7**).

Competing Interests

The authors have declared that no competing interest exists.

References

1. Wada K, Yu W, Elazizi M, Barakat S, Ouimet MA, Rosario-Meléndez R, et al. Locally delivered salicylic acid from a poly(anhydride-ester): Impact on diabetic bone regeneration. J Control Release. 2013; 171: 33-7.

2. Miao S, Guo X, Bai C, Zhou W, Wu Y, Ding W, et al. Freeze-derived microporous biomaterials for tissue engineering applications. Smart Med. 2026; 5: e70035.
3. Xie E, Yuan Z, Chen Q, Hu J, Li J, Li K, et al. Programmed transformation of osteogenesis microenvironment by a multifunctional hydrogel to enhance repair of infectious bone defects. Adv Sci (Weinh). 2025; 12: e2409683.
4. Li L, Li Q, Gui L, Deng Y, Wang L, Jiao J, et al. Sequential gastrodin release pu/n-ha composite scaffolds reprogram macrophages for improved osteogenesis and angiogenesis. Bioact Mater. 2023; 19: 24-37.
5. Zhou W, Liu Y, Nie X, Zhu C, Xiong L, Zhou J, et al. Peptide-based inflammation-responsive implant coating sequentially regulates bone regeneration to enhance interfacial osseointegration. Nat Commun. 2025; 16: 3283.
6. McDermott AM, Herberg S, Mason DE, Collins JM, Pearson HB, Dawahare JH, et al. Recapitulating bone development through engineered mesenchymal condensations and mechanical cues for tissue regeneration. Sci Transl Med. 2019; 11: eaav7756.
7. Li Y, Liu Z, Tang Y, Feng W, Zhao C, Liao J, et al. Schnurri-3 regulates bmp9-induced osteogenic differentiation and angiogenesis of human amniotic mesenchymal stem cells through runx2 and vegf. Cell Death Dis. 2020; 11: 72.
8. Wang Y, Hu Y, Lan S, Chen Z, Zhang Y, Guo X, et al. A recombinant parathyroid hormone-related peptide locally applied in osteoporotic bone defect. Adv Sci (Weinh). 2023; 10: e2300516.
9. Fang L, Liu Z, Wang C, Shi M, He Y, Lu A, et al. Vascular restoration through local delivery of angiogenic factors stimulates bone regeneration in critical size defects. Bioact Mater. 2024; 36: 580-94.
10. Bai B, Liu Y, Huang J, Wang S, Chen H, Huo Y, et al. Tolerant and rapid endochondral bone regeneration using framework-enhanced 3d biomineralized matrix hydrogels. Adv Sci (Weinh). 2024; 11: e2305580.
11. Zhang Y, Zheng Z, Zhu S, Xu L, Zhang Q, Gao J, et al. Electroactive electrospun nanofibrous scaffolds: Innovative approaches for improved skin wound healing. Adv Sci (Weinh). 2025; 12: e2416267.
12. Huang D, Cai L, Li N, Zhao Y. Ultrasound-trigged micro/nanorobots for biomedical applications. Smart Med. 2023; 2: e20230003.
13. Wang Y, Guo J, Cao X, Zhao Y. Developing conductive hydrogels for biomedical applications. Smart Med. 2024; 3: e20230023.
14. Heng BC, Bai Y, Li X, Lim LW, Li W, Ge Z, et al. Electroactive biomaterials for facilitating bone defect repair under pathological conditions. Adv Sci (Weinh). 2023; 10: e2204502.
15. Shang S, Zheng F, Tan W, Xing Z, Chen S, Peng F, et al. Piezoelectric biomaterial with advanced design for tissue infection repair. Adv Sci (Weinh). 2025; 12: e2413105.
16. Zhang H, Zhao Z, Wu C. Bioactive inorganic materials for innervated multi-tissue regeneration. Adv Sci (Weinh). 2025; 12: e2415344.
17. Sharma M, Madras G, Bose S. Process induced electroactive β-polymorph in pvdf: Effect on dielectric and ferroelectric properties. Phys Chem Chem Phys. 2014; 16: 14792-9.
18. Jonkman JEN, Cathcart JA, Xu F, Bartolini ME, Amon JE, Stevens KM, et al. An introduction to the wound healing assay using live-cell microscopy. Cell Adh Migr. 2014; 8: 440-51.
19. Sawauchi K, Fukui T, Oe K, Kumabe Y, Oda T, Yoshikawa R, et al. Low-intensity pulsed ultrasound promotes osteogenic differentiation of reamer-irrigator-aspirator graft-derived cells in vitro. Ultrasound Med Biol. 2022; 48: 313-22.
20. Palanisamy P, Alam M, Li S, Chow SKH, Zheng Y-P. Low-intensity pulsed ultrasound stimulation for bone fractures healing. J Ultrasound Med. 2022; 41: 547-63.
21. Mundi R, Petis S, Kaloty R, Shetty V, Bhandari M. Low-intensity pulsed ultrasound: Fracture healing. Indian J Orthop. 2009; 43: 132-40.
22. Pounder NM, Harrison AJ. Low intensity pulsed ultrasound for fracture healing: A review of the clinical evidence and the associated biological mechanism of action. Ultrasonics. 2008; 48: 330-8.
23. Song R, Xia G, Xing X, He L, Zhao Q, Ma Z. Modification of polymorphisms in polyvinylidene fluoride thin films via water and hydrated salt. J Colloid Interface Sci. 2013; 401: 50-7.
24. Jana S, Garain S, Sen S, Mandal D. The influence of hydrogen bonding on the dielectric constant and the piezoelectric energy harvesting performance of hydrated metal salt mediated pvdf films. Phys Chem Chem Phys. 2015; 17: 17429-36.
25. Kong Y, Liu F, Ma B, Duan J, Yuan W, Sang Y, et al. Wireless localized electrical stimulation generated by an ultrasound-driven piezoelectric discharge regulates proinflammatory macrophage polarization. Adv Sci (Weinh). 2021; 8: 2100962.
26. Putzeys T, Wübbenhorst M. Asymmetric polarization and hysteresis behaviour in ferroelectric p(vdf–trfe) (76 : 24) copolymer thin films spatially resolved via limm. Phys Chem Chem Phys. 2015; 17: 7767-74.
27. Furukawa T, Date M, Fukada E. Hysteresis phenomena in polyvinylidene fluoride under high electric field. J Appl Phys. 1980; 51: 1135-41.
28. Martins P, Lopes AC, Lanceros-Mendez S. Electroactive phases of poly(vinylidene fluoride): Determination, processing and applications. Prog Polym Sci. 2014; 39: 683-706.
29. Wang S, Li Q. Design, synthesis and processing of pvdf-based dielectric polymers. IET Nanodielectrics. 2018; 1: 80-91.
30. Fukada E, Furukawa T. Piezoelectricity and ferroelectricity in polyvinylidene fluoride. Ultrasonics. 1981; 19: 31-9.
31. Schönlein R, Bhattarai P, Raef M, Larrañaga X, Poudel A, Biggs M, et al. Piezoelectric polylactic acid-based biomaterials: Fundamentals, challenges and opportunities in medical device design. Biomaterials. 2026; 324: 123522.
32. Yang C, Zhao M, Yu N, Wang S, Li Y, Chen H, et al. Novel degradable piezoelectric-induced phbv/cs/ha scaffolds to achieve dual effects of endogenous osteogenesis and antibacterial properties by piezoelectric stimulation and ultrasonic action. Chem Eng J. 2025; 519: 165133.
33. Ni X, Cui Y, Salehi M, Nai MLS, Zhou K, Vyas C, et al. Piezoelectric biomaterials for bone regeneration: Roadmap from dipole to osteogenesis. Adv Sci (Weinh). 2025; 12: e14969.
34. Han J, Li Z, Du J, Zhang Q, Ge S, Liu H, et al. Natural collagen scaffold with intrinsic piezoelectricity for enhanced bone regeneration. Mater Today Bio. 2025; 31: 101532.
35. Mirghaffari M, Mahmoodiyan A, Mahboubizadeh S, Shahbazi A, Soleimani Y, Mirghaffari S, et al. Electro-spun piezoelectric plla smart composites as a scaffold on bone fracture: A review. Regen Ther. 2025; 28: 591-605.
36. Omar O, Engstrand T, Kihlström Burenstam Linder L, Åberg J, Shah FA, Palmquist A, et al. In situ bone regeneration of large cranial defects using synthetic ceramic implants with a tailored composition and design. Proc Natl Acad Sci U S A. 2020; 117: 26660-71.
37. Yuan Y, Xu Y, Mao Y, Liu H, Ou M, Lin Z, et al. Three birds, one stone: An osteo-microenvironment stage-regulative scaffold for bone defect repair through modulating early osteo-immunomodulation, middle neovascularization, and later osteogenesis. Adv Sci (Weinh). 2024; 11: e2306428.
38. Hamlet SM, Lee RSB, Moon HJ, Alfarsi MA, Ivanovski S. Hydrophilic titanium surface-induced macrophage modulation promotes pro-osteogenic signalling. Clin Oral Implants Res. 2019; 30: 1085-96.
39. Wang Y, Sun SK, Liu Y, Zhang Z. Advanced hitchhiking nanomaterials for biomedical applications. Theranostics. 2023; 13: 4781-801.
40. Lu Y, Bai Y, Wu L, Tang L, Heng BC, Xu M, et al. Lipus-activated piezoelectric sutures exert antibacterial and pro-regenerative effects to promote wound healing. Dent Res. 2026; 1: 100044.
41. Yin Y, Cai Y, Dang P, Zeng W, Wang L, Yan X, et al. A near-infrared regulated programmable multi-mode periosteum scaffold for sequential healing of infected bone defects. Bioact Mater. 2026; 63: 56-72.
42. Li Q, Li C, Yan J, Zhang C, Jiang Y, Hu X, et al. Evenly distributed microporous structure and e7 peptide functionalization synergistically accelerate osteogenesis and angiogenesis in engineered periosteum. Adv Sci (Weinh). 2025; 12: e2406084.
43. Li Y, Hoffman MD, Benoit DSW. Matrix metalloproteinase (mmp)-degradable tissue engineered periosteum coordinates allograft healing via early stage recruitment and support of host neurovasculature. Biomaterials. 2021; 268: 120535.
44. Liu YL, Tang XT, Shu HS, Zou W, Zhou BO. Fibrous periosteum repairs bone fracture and maintains the healed bone throughout mouse adulthood. Dev Cell. 2024; 59: 1192-209.e6.
45. Sparks DS, Savi FM, Dlaska CE, Saifzadeh S, Brierly G, Ren E, et al. Convergence of scaffold-guided bone regeneration principles and microvascular tissue transfer surgery. Sci Adv. 2023; 9: eadd6071.
46. Sharifi M, Salehi M, Ebrahimi-Barough S, Alizadeh M, Jahromi HK, Kamalabadi-Farahani M. Synergic effects of core-shell nanospheres and magnetic field for sciatic nerve regeneration in decellularized artery conduits with schwann cells. J Nanobiotechnology. 2024; 22: 776.
47. Mao M, Qu X, Zhang Y, Gu B, Li C, Liu R, et al. Leaf-venation-directed cellular alignment for macroscale cardiac constructs with tissue-like functionalities. Nat Commun. 2023; 14: 2077.
48. Zhang H, Wang K, Xu D, Miao S, Dai Y, Liu P, et al. Conductive nerve conduits with orientated topological structures from ice-templating technology. Smart Med. 2025; 4: e70012.
49. Jorba I, Gussenhoven S, van der Pol A, Groenen BGW, van Zon M, Goumans MJ, et al. Steering cell orientation through light-based spatiotemporal modulation of the mechanical environment. Biofabrication. 2024; 16: 035011.
50. Kong Y, Duan J, Liu F, Han L, Li G, Sun C, et al. Regulation of stem cell fate using nanostructure-mediated physical signals. Chem Soc Rev. 2021; 50: 12828-72.

51. Zhang M, Peng X, Xu H, Sun X, Liu Y, Li Q, et al. Photoacoustic imaging-guided self-adaptive hyperthermia supramolecular cascade nano-reactor for diabetic periodontal bone regeneration. Adv Sci (Weinh). 2024; 11: e2404143.
52. Chen Y, Zhang Q, Yang S, Li G, Shi C, Hu X, et al. Formulate adaptive biphasic scaffold via sequential protein-instructed peptide co-assembly. Adv Sci (Weinh). 2024; 11: e2401478.
53. Wang X, Zeng J, Gan D, Ling K, He M, Li J, et al. Recent strategies and advances in hydrogel-based delivery platforms for bone regeneration. Nanomicro Lett. 2024; 17: 73.
54. Mizuno M, Kuboki Y. Osteoblast-related gene expression of bone marrow cells during the osteoblastic differentiation induced by type i collagen. J Biochem. 2001; 129: 133-8.
55. Bailey S, Karsenty G, Gundberg C, Vashishth D. Osteocalcin and osteopontin influence bone morphology and mechanical properties. Ann N Y Acad Sci. 2017; 1409: 79-84.
56. Depalle B, McGilvery CM, Nobakhti S, Aldegaither N, Shefelbine SJ, Porter AE. Osteopontin regulates type i collagen fibril formation in bone tissue. Acta Biomater. 2021; 120: 194-202.
57. Demir-Oğuz Ö, Boccaccini AR, Loca D. Injectable bone cements: What benefits the combination of calcium phosphates and bioactive glasses could bring? Bioact Mater. 2023; 19: 217-36.
58. Wang C, Liu J, Min S, Liu Y, Liu B, Hu Y, et al. The effect of pore size on the mechanical properties, biodegradation and osteogenic effects of additively manufactured magnesium scaffolds after high temperature oxidation: An in vitro and in vivo study. Bioact Mater. 2023; 28: 537-48.
59. Cutiongco MFA, Jensen BS, Reynolds PM, Gadegaard N. Predicting gene expression using morphological cell responses to nanotopography. Nat Commun. 2020; 11: 1384.
60. Wu J, Yun Z, Song W, Yu T, Xue W, Liu Q, et al. Highly oriented hydrogels for tissue regeneration: Design strategies, cellular mechanisms, and biomedical applications. Theranostics. 2024; 14: 1982-2035.
61. Zhou Y, Zhang Z, Zhou C, Ma Y, Huang H, Liu J, et al. Nanotechnology-fortified manipulation of cell ca(2+) signaling. Small Sci. 2024; 4: 2400169.
62. Zhong YT, Liao HB, Ye ZQ, Jiang HS, Li JX, Ke LM, et al. Eurycomanone stimulates bone mineralization in zebrafish larvae and promotes osteogenic differentiation of mesenchymal stem cells by upregulating akt/gsk-3β/β-catenin signaling. J Orthop Translat. 2023; 40: 132-46.
63. Yao G, Kang L, Li C, Chen S, Wang Q, Yang J, et al. A self-powered implantable and bioresorbable electrostimulation device for biofeedback bone fracture healing. Proc Natl Acad Sci USA. 2021; 118: e2100772118.
64. Tian P, Zhao L, Kim J, Li X, Liu C, Cui X, et al. Dual stimulus responsive borosilicate glass (bsg) scaffolds promote diabetic alveolar bone defectsrepair by modulating macrophage phenotype. Bioact Mater. 2023; 26: 231-48.
65. Li R, Zhou C, Chen J, Luo H, Li R, Chen D, et al. Synergistic osteogenic and angiogenic effects of kp and qk peptides incorporated with an injectable and self-healing hydrogel for efficient bone regeneration. Bioact Mater. 2022; 18: 267-83.
66. Ren X, Zhuang H, Zhang Y, Zhou P. Cerium oxide nanoparticles-carrying human umbilical cord mesenchymal stem cells counteract oxidative damage and facilitate tendon regeneration. J Nanobiotechnology. 2023; 21: 359.
67. Libako P, Nowacki W, Castiglioni S, Mazur A, Maier JA. Extracellular magnesium and calcium blockers modulate macrophage activity. Magnes Res. 2016; 29: 11-21.
68. Zheltova AA, Kharitonova MV, Iezhitsa IN, Spasov AA. Magnesium deficiency and oxidative stress: An update. Biomedicine (Taipei). 2016; 6: 20.
69. Joo S, Gwon Y, Kim S, Park S, Kim J, Hong S. Piezoelectrically and topographically engineered scaffolds for accelerating bone regeneration. ACS Appl Mater Interfaces. 2024; 16: 1999-2011.
70. Silva CA, Fernandes MM, Ribeiro C, Lanceros-Mendez S. Two- and three-dimensional piezoelectric scaffolds for bone tissue engineering. Colloids Surf B Biointerfaces. 2022; 218: 112708.
71. Tandon B, Aguilar Cosme JR, Xue R, Srirussamee K, Aguilar-Tadeo J, Ballestrem C, et al. Co-stimulation with piezoelectric pvdf films and low intensity pulsed ultrasound enhances osteogenic differentiation. Biomater Adv. 2025; 173: 214283.
72. Wu H, Wei X, Liu Y, Dong H, Tang Z, Wang N, et al. Dynamic degradation patterns of porous polycaprolactone/β-tricalcium phosphate composites orchestrate macrophage responses and immunoregulatory bone regeneration. Bioact Mater. 2023; 21: 595-611.
73. Liu S, Manshaii F, Chen J, Wang X, Wang S, Yin J, et al. Unleashing the potential of electroactive hybrid biomaterials and self-powered systems for bone therapeutics. Nanomicro Lett. 2024; 17: 44.
74. Zhang X, Chen Q, Mao X. Magnesium enhances osteogenesis of bmscs by tuning osteoimmunomodulation. Biomed Res Int. 2019; 2019: 7908205.
75. Qiao W, Wong KHM, Shen J, Wang W, Wu J, Li J, et al. Trpm7 kinase-mediated immunomodulation in macrophage plays a central role in magnesium ion-induced bone regeneration. Nat Commun. 2021; 12: 2885.
76. Liu Y-B, Liu X, Li X-F, Qiao L, Wang H-L, Dong Y-F, et al. Multifunctional piezoelectric hydrogels under ultrasound stimulation boost chondrogenesis by recruiting autologous stem cells and activating the ca2+/cam/can signaling pathway. Bioact Mater. 2025; 50: 344-63.
77. McWhorter FY, Wang T, Nguyen P, Chung T, Liu WF. Modulation of macrophage phenotype by cell shape. Proc Natl Acad Sci U S A. 2013; 110: 17253-8.
78. Tang J, Wang X, Lin X, Wu C. Mesenchymal stem cell-derived extracellular vesicles: A regulator and carrier for targeting bone-related diseases. Cell Death Discov. 2024; 10: 212.
79. Xue H, Zhang Z, Lin Z, Su J, Panayi AC, Xiong Y, et al. Enhanced tissue regeneration through immunomodulation of angiogenesis and osteogenesis with a multifaceted nanohybrid modified bioactive scaffold. Bioact Mater. 2022; 18: 552-68.
80. Schlundt C, El Khassawna T, Serra A, Dienelt A, Wendler S, Schell H, et al. Macrophages in bone fracture healing: Their essential role in endochondral ossification. Bone. 2018; 106: 78-89.
81. Luo Y, Liu Y, Wang B, Zhou J, Xiao D, Chen W. Immunomodulation-based multifunctional decellularized matrix bioink derived from m2 macrophages remodels the bone microenvironment via neurogenesis and angiogenesis. Adv Funct Mater. 2026; 36: e04709.
82. Wang M, Su Q, Wu Y, Liang X, Zhou F, Jing Y, et al. Hydrogels for bone repair: Construction strategies and applications. Smart Med. 2026; 5: e70036.
83. Ha DP, Lee AS. Insulin-like growth factor 1-receptor signaling stimulates grp78 expression through the pi3k/akt/mtor/atf4 axis. Cell Signal. 2020; 75: 109736.
84. Habibian JS, Jefic M, Bagchi RA, Lane RH, McKnight RA, McKinsey TA, et al. Dusp5 functions as a feedback regulator of tnfα-induced erk1/2 dephosphorylation and inflammatory gene expression in adipocytes. Sci Rep. 2017; 7: 12879.
85. Cao M, Chen P, Peng B, Cheng Y, Xie J, Hou Z, et al. The transcription factor elf4 alleviates inflammatory bowel disease by activating il1rn transcription, suppressing inflammatory th17 cell activity, and inducing macrophage m2 polarization. Front Immunol. 2023; 14: 1270411.
86. Jadaun PK, Zhang S, Koedam M, Demmers J, Chatterjee S, van Leeuwen JP, et al. Inhibition of hypoxia-induced mucin 1 alters the proteomic composition of human osteoblast-produced extracellular matrix, leading to reduced osteogenic and angiogenic potential. J Cell Physiol. 2022; 237: 1440-54.
87. Li W, Peng J, Yao D, Rao B, Xia Y, Wang Q, et al. The structural basis for the collagen processing by human p3h1/crtap/ppib ternary complex. Nat Commun. 2024; 15: 7844.
88. Shang J, Yu Z, Xiong C, Zhang J, Gong J, Yu C, et al. Resistin targets taz to promote osteogenic differentiation through pi3k/akt/mtor pathway. iScience. 2023; 26: 107025.
89. Yahiro Y, Maeda S, Morikawa M, Koinuma D, Jokoji G, Ijuin T, et al. Bmp-induced atoh8 attenuates osteoclastogenesis by suppressing runx2 transcriptional activity and reducing the rankl/opg expression ratio in osteoblasts. Bone Res. 2020; 8: 32.
90. Dutta SD, Ganguly K, Patil TV, Randhawa A, Lim KT. Unraveling the potential of 3d bioprinted immunomodulatory materials for regulating macrophage polarization: State-of-the-art in bone and associated tissue regeneration. Bioact Mater. 2023; 28: 284-310.
91. Jun JH, Yoon W-J, Seo S-B, Woo K-M, Kim G-S, Ryoo H-M, et al. Bmp2-activated erk/map kinase stabilizes runx2 by increasing p300 levels and histone acetyltransferase activity*. J Biol Chem. 2010; 285: 36410-9.
92. Zhang F, Lv M, Wang S, Li M, Wang Y, Hu C, et al. Ultrasound-triggered biomimetic ultrashort peptide nanofiber hydrogels promote bone regeneration by modulating macrophage and the osteogenic immune microenvironment. Bioact Mater. 2024; 31: 231-46.
93. Srirussamee K, Mobini S, Cassidy NJ, Cartmell SH. Direct electrical stimulation enhances osteogenesis by inducing bmp2 and spp1 expressions from macrophages and preosteoblasts. Biotechnol Bioeng. 2019; 116: 3421-32.
94. Komori T, Yagi H, Nomura S, Yamaguchi A, Sasaki K, Deguchi K, et al. Targeted disruption of cbfa1 results in a complete lack of bone formation owing to maturational arrest of osteoblasts. Cell. 1997; 89: 755-64.
95. Lai Y, Guo Y, Liao C, Mao C, Liu J, Ren C, et al. Osteoclast differentiation and dynamic mrna expression during mice embryonic palatal bone development. Scientific Reports. 2023; 13: 15170.
96. Takayanagi H, Kim S, Koga T, Nishina H, Isshiki M, Yoshida H, et al. Induction and activation of the transcription factor nfatc1 (nfat2) integrate rankl signaling in terminal differentiation of osteoclasts. Developmental Cell. 2002; 3: 889-901.

97. Chen L, Yao Z, Zhang S, Tang K, Yang Q, Wang Y, et al. Biomaterial-induced macrophage polarization for bone regeneration. Chin Chem Lett. 2023; 34: 107925.